A COMPARISON OF TWO INVERSION METHODS FOR DETERMINATION OF SAND CONCENTRATION AND SIZE FROM MULTIFREQUENCY ACOUSTIC BACKSCATTER

ANNA M. CRAWFORD

A Comparison of Two Inversion Methods for Determination of Sand Concentration and Size from Multifrequency Acoustic Backscatter

©Anna M. Crawford, B.Sc.

A thesis submitted to the School of Graduate Studies in partial fulfillment of the requirements for the degree of Master of Science

Depar'ment of Physics

Memorial University of Newfoundland

St. John's, Newfoundland

January, 1992

ISBN 0-315-82655-X

Abstract

RASTRAN (Remote Acoustic Sediment TRANsport measurement) System 1 has been used in laboratory trials and deployed in nearshore locations as part of several field experiments. The system operates at three frequencies, 1, 2.25 and 5 MHz, over a range of approximately 1 m, with resolution of about 2 cm. A central concern has been the probable errors in suspended sediment concentration and size derived from the backscatter data. An inversion algorithm based on the differences in backscattered pressure amplitude at the three frequencies has been developed. Laboratory experiments, measuring multifrequency backscatter from a turbulent sediment-carrying jet, have been used to calibrate the system and to test the inversion algorithm . Concentration and sizes inverted from field and laboratory data are compared with results from a previously developed algorithm based on signal ratios. Inverted concentrations are also compared with Optical Backscatter Sensor (OBS) data collected during the field experiment. This latest inversion scheme is less sensitive to errors arising from low signal levels, increasing the size/concentration measurement range to regions of lower concentration. The concentration results agree well with the independent OBS data.

Acknowledgements

Firstly, I wish to thank Dr. Alex Hay for offering the right amount of supervision at the right times. The vast amount of work done by Dr. J. Sheng, upon which a large portion of this work has been based, cannot go unmentioned. Mr. Rod Campbell supplied computing know-how and management of the system-from-hell. Finally, discussion with Mr. Doug Wilson on many occasions has been greatly appreciated.

On a more personal note, I wish to thank my father for teaching me the real value of the day – thank you for not going gentle into that good night[1].

[1] From "Do not go gentle into that good night", *Dylan Thomas Collected Poems 1934-1953*, Davies, W. and R. Maud, eds., J. M. Dent and Sons Ltd., London, 1988.

Contents

List of Figures 4

List of Tables 8

List of Symbols 9

1 Introduction **12**

2 Measurement with RASTRAN System 1 **17**

2.1 Laboratory Experiments 20

2.2 Field Deployment and Experiments 25

3 Acoustic Backscattering Theory **30**

3.1 The Acoustic Backscattering Form Factor — $|f_\infty(X)|$ 38

3.2 Scattering Attenuation Correction 45

3.3 The Geometric Correction Factor — F 47

4 Inversion Algorithm **49**

4.1 Calculation of Scattering Attenuation 56

4.2 Comparison With an Earlier Inversion Scheme 56

5 Laboratory Results **59**

5.1 Geometric Considerations in the Tank Experiments 63

5.2 Examination of Scattering Attenuation 67

5.3 Examination of the Form Factor 75

5.4 Comparison with Results of a Previous Inversion Method . . 77

5.5 Averaging and Examination of the Stability of the Jet 81

6 Field Results **86**

6.1 Comparison of Inverted Concentration with OBS133 Measurements 87

6.2 Averaged Size and Concentration Profiles 88

7 Conclusions **106**

References **109**

List of Figures

2.1 Block diagram of RASTRAN System 1, including the EX-ADAC system. 19

2.2 Configuration of laboratory tank setup, side-on [from Hay, 1991]. 21

2.3 RASTRAN nearshore field deployment: profile of the beach topography at Stanhope Lane Beach [from Sheng and Hay, 1991]. 26

2.4 RASTRAN nearshore field deployment: side and plan views of the sensor array. 27

3.1 Backscattering geometry for a monostatic system [from Sheng, 1990]. 32

3.2 Backscatter form factor, $|f_{\infty s}|$, for natural sand grains in water. 40

3.3 Rational fraction fit to experimental backscattering form factor data. 43

3.4 Percentage difference between the semi-empirical and rational fraction fit form factors. 44

4.1 Flow chart of the inversion algorithm. 52

4.2 ϵ_{max} versus diameter. 55

5.1 Comparison of measured and inverted laboratory data. 61

5.1 Comparison of measured and inverted laboratory data. 62

5.2 Inverted size profiles of the jet for a range of concentrations and sizes D = 360 μm (QLB sand) and 157 μm (PEI sand). . 64

5.2 Inverted size profiles of the jet for a range of concentrations, D = 139 μm (BWB sand). 65

5.3 Comparison of measured laboratory data with calculated values, including scattering attenuation. 68

5.4 Measured and calculated scattering attenuation across the full width of the jet. 70

5.5 Measured and calculated scattering attenuation across half the jet. 72

5.6 Concentration profiles across the jet. 74

5.7 Comparison of measured and inverted laboratory data using the rational fraction fit form factor. 78

5.8 Comparison of measured and inverted jet centreline concentration and size using Sheng's algorithm. 79

5.9 Sample standard deviation as a function of sample size. . . . 83

5.10 Time series of concentration at range 53 cm. Sieved sand size is 196 μm and mean concentration (dotted line) is 0.83 g/l. . 85

6.1 Comparison between inverted and OBS133 measured concentration. 89

6.1 Comparison between inverted and OBS133 measured concentration obtained by Sheng and Hay [1991]. 90

6.2 Size profiles averaged over complete runs and standard error calculated using semi-empirical form factor. 92

6.3 Size profiles averaged over complete runs and standard error calculated using rational fraction fit form factor. 93

6.4 Size profiles averaged over complete runs and standard error from Sheng and Hay [1991]. 94

6.5 Averaged vertical profiles of concentration from field data. . . 97

6.6 Similar concentration profiles from Sheng's inversion algorithm [from Sheng and Hay, 1991]. 98

6.7 4-run averaged profiles of size and concentration for runs 299.025-.028. 100

6.8 4-run averaged profiles of size showing standard error for runs 299.025-.028. 101

6.9 4-run averaged profile of size from Sheng's algorithm showing standard error. 102

6.10 Percent difference between size and concentration estimates using the two different form factors. 104

List of Tables

2.1 Physical properties of particles used in laboratory experiments. 24

2.2 Size characteristics of sieved sand samples. 24

2.3 Size characteristics of natural sand types. 25

2.4 RASTRAN data files selected for comparisons. 29

3.1 Properties of transducers used with RASTRAN. 34

3.2 System sensitivity constants for RASTRAN transducers. . . . 37

6.1 Distances for RASTRAN-OBS133 concentration comparison. 87

List of Symbols

a	scattering particle radius
a_o	radius of transducer face
a_o^*	effective radius of transducer face
c	sound speed in fluid
c_c'	compressional wave speed in scatterers
c_s'	shear wave speed in scatterers
D	transducer directivity
$\|f_{\infty s}\|$	semi-empirical far-field backscattering form factor
$\|f_{\infty g}\|$	far-field backscattering form factor for glass beads
$\|f_{\infty r}\|$	rational fraction fit backscattering form factor
k_c	compressional wave number in ambient fluid
M	mass density of scatterers
N	number density of scatterers

$n(a)$	distribution function for size
p_i	incident pressure at scatterer
p_s	scattered pressure at scatterer
r	range from center of transducer
r_o	range to center of detected volume
R_c	far-field critical range
S_M, S_N	system calibration factors
$< v^2 >$	mean squared voltage output from tranducers
V_d	detected volume
X	$= k_c a$, non-dimensional radius of scatterer
α	combined attenuation due to water and scatterers
α_o	attenuation due to ambient fluid
α_s	attenuation due to scatterers
β_o	3-dB beamwidth for transducer beam pattern
β_m	beamwidth to first zero of D
Δ	integrated scattering attenuation
ϵ_{mn}	Equation 32
λ	wavelength of sound in fluid
ρ_o	density of ambient fluid

ρ_o'	density of scatterers
σ_g	width of log-normal size distribution for sand size
Σ_s	total scattering cross section
τ	acoustic pulse duration

Chapter 1

Introduction

Various means have been used to obtain field measurements of sediment transport in nearshore environments. *In situ* and remote techniques have associated advantages and disadvantages. It is difficult to design a direct sampling system which does not disrupt natural flow, has reasonable temporal resolution and is robust enough to withstand sometimes violent wave action. Moderate success has been obtained using pumps [Jensen and Sorensen, 1972; Renger, 1986], and diver-operated traps [Kana, 1976]. Other measurements have been carried out using sensors which detect impacting sand grains [Soulsby *et al.*, 1985].

Optical methods offer minimal disruption of the area under observa-

tion except very near the bed, as well as much greater temporal resolution. However, careful calibration of these instruments is necessary to obtain absolute measures. Optical attenuation devices, such as that reported by Brenninkmeyer [1976], have obtained reliable vertical density distribution measurements. Optical backscatter measurements have been widely used with good results [Downing *et al.*, 1981; Hanes and Huntley, 1986], though these instruments generally monitor a single point above the seabed.

Acoustic methods have been frequently used for the detection of suspended material in the ocean over the past decade. These offer the same advantages as optical methods: fine temporal resolution with very little disturbance of the area under study. The main advantage of acoustic over optical systems is that, due to the speed of sound in water being much less than that of light, range gating is feasible so acoustic systems can be used to obtain backscatter profiles with centimeter resolution. Most development has been in active systems which survey an area with transmitted sound. These systems can measure attenuation or intensity of scattered energy. The Ultrasonic Doppler Scatterometer (UDS) reported by Jansen [1979] and Schaafsma and der Kinderen [1985] is an example of an active system which measures concentration and velocity simultaneously from sound scattered by moving particles. Less common are passive systems, such as

that described by Thorne [1986] which detects self-generated noise -- the acoustic energy released when particles collide as they move along the bed.

The RASTRAN (Remote Acoustic Sediment TRANsport system) System 1 is a multi-frequency acoustic backscatter measurement system operating at 1, 2.25 and 5 MHz. Other earlier backscatter measuring systems [Thorne *et al.*, 1991; Young *et al.*, 1982; Lynch, 1985; Hanes *et al.*, 1988; Libicki and Bedford, 1989; Lynch *et al.*, 1991] operated at a single frequency. Simultaneous backscatter at several frequencies offers more information about the suspended scatterers and, in principle, resolves the size–concentration ambiguity inherent in single frequency backscatter.

In wave–dominated areas, sediment is carried by bedload and suspended load [Sleath, 1984]. Bedload comprises those particles which move intermittently along the bed with the maximum impulse of the wave action and come to rest during each wave period. Suspended load includes those particles which have been lifted up from the bottom and can remain suspended by turbulence for several wave cycles. Accurate determination of concentration, coupled with velocity measurement, is necessary to extract suspended sediment transport. Size profiles are a significant contribution to understanding of transport, as settling velocity is determined primarily from particle diameter [Murray, 1970]. Sediment transport by bedload is largely confined

to the near-bed region where concentrations of scatterers are very high, out of the realm of the present type of acoustic measurement.

Previous efforts by other groups have been almost exclusively directed toward obtaining concentration only, relying on assumptions, grab sampling or *in situ* methods such as laser diffractometry for determination of size. Both of the latter are counter-productive to the main goals of remote sensing mentioned above. Lynch and Agrawal [1991] have developed a size inversion method based on the size-dependence of particle fall velocity from established equilibrium boundary layer profiles. Their procedure is suitable for use with both optical transmissometry or single-frequency acoustic backscatter systems, though their results are dependent on the specific boundary layer model used. Multifrequency backscatter has been used with some success in determining size distributions of oceanic zooplankton populations [Holliday and Pieper, 1980; Kristensen and Dalen, 1986] and bubbles [Medwin, 1970 and 1977].

An inversion algorithm for size and concentration has been developed for use with the multifrequency backscatter data collected using RASTRAN System 1. The extraction of size is based on the difference between backscattered intensity at 3 different frequencies. Concentration is calculated from the estimated size. Previous work [Sheng, 1990; Sheng and Hay, 1991] used

an earlier algorithm based on matching ratios of signal levels to theoretical ratios. This scheme breaks down at low signal levels. The new algorithm is not prone to this error and as a result the time-averaged inverted profiles are more stable in regions of low concentration.

The following contains a description of RASTRAN in laboratory and field deployments. The basic theory of acoustic backscatter from a collection of randomly oriented particles is discussed briefly, with mention of factors specific to RASTRAN. The inversion algorithm is described and compared to the algorithm developed by Sheng. Results from laboratory and field experiments will be presented, with further comparison to previous results.

Chapter 2

Measurement with RASTRAN System 1

The RASTRAN system has been used in both field and laboratory experiments. The on-land or "dry" part of the system remains largely the same in both cases. A description of the specific underwater or "wet" system deployment in both cases will be given in the following sections. A more detailed description of the system is given by Hay *et al.* [1988].

Transmitted signals are generated by Mesotech Model 810 immersible acoustic sounders operating at the three frequencies: 1, 2.25 and 5 MHz. The received signal is TVG (Time-Variable Gain) amplified, correcting for

attenuation and spherical spreading, and heterodyned down to 455 kHz. The system is shown in Figure 2.1 in diagramatic form. Acquisition of the data, as well as triggering of the transducers, is controlled by EXADAC (an Expandable Acoustic Data ACquisition system)[Hay *et al.*, 1988]. EXADAC consists of a CAMAC (Computer Automated Measurement and Control) crate which controls several plug-in modules: a LeCroy 8501 programmable clock, a LeCroy 6810 programmable transient recorder and a LeCroy 8901A GPIB controller which interfaces with an external microcomputer. The acoustic signals are full-wave rectified and low-pass filtered in an envelope detector before A/D conversion at 200 kHz. Some averaging is done before data is stored in order to reduce statistical fluctuations [Hay, 1983]. Usually, a 4-ping ensemble-average is performed, followed by block-averaging of 3-to-5 adjacent samples.

Large amounts of acoustic data are accumulated in very short periods of time. In the field experiments, for example, a single 6.5 minute run with 4 channels produced 1.2 MBytes of binary data. In the past, 9-track magnetic tape and floppy disks have been used to store the data. Currently, Digital Audio Tape (DAT) systems are being used as a means of efficiently dealing with the large quantities of information.

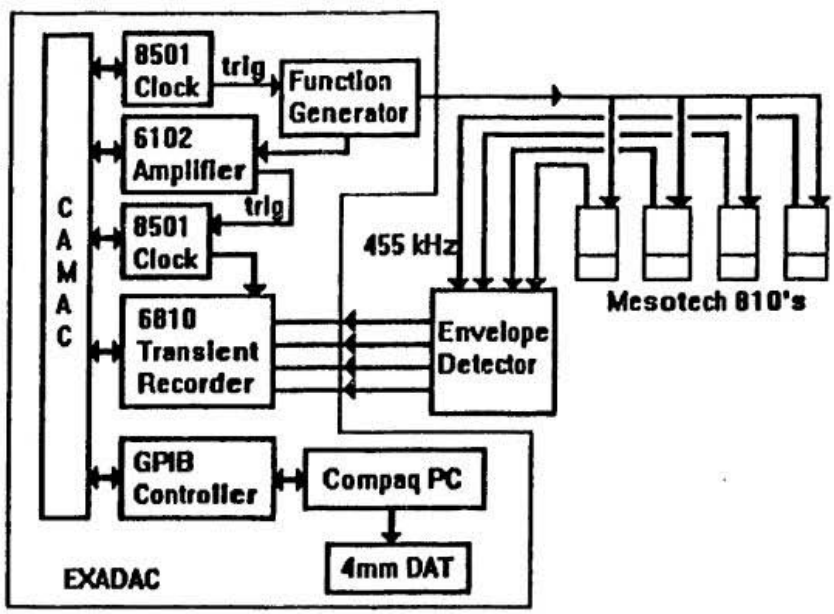

Figure 2.1: Block diagram of RASTRAN System 1, including the EXADAC system.

2.1 Laboratory Experiments

Laboratory trials both for calibration of the system and as experiments in their own right have been conducted in a large tank containing a recirculating sediment laden jet. A diagram of the tank and the RASTRAN "wet" system is shown in Figure 2.2.

The "dry" part of RASTRAN in this application is as described previously. Controlling software ensemble-average the digitized data from four backscatter profiles for consecutive pulses (transmitted at 10 ms intervals), and block-averaged over 3 adjacent sample points, so that each recorded data point represents 12 samples. In this mode, the range resolution is 1.1 cm, and the system acquires averaged backscatter profiles at a rate of 6.5 Hz [Hay, 1991].

The transducers are mounted as shown in Figure 2.2. Attenuation and beam pattern measurements are obtained with a 2 mm diameter probe hydrophone at 2.25 MHz and the 4.5 MHz first harmonic. Only those results for the fundamental frequency have been used here. Velocity in the jet was determined with a Marsh-McBirney Model 523 electromagnetic current meter with sensors mounted on a spherical probe 1.3 cm in diameter.

The jet itself is supplied by a pump system. Nozzle velocity is controlled

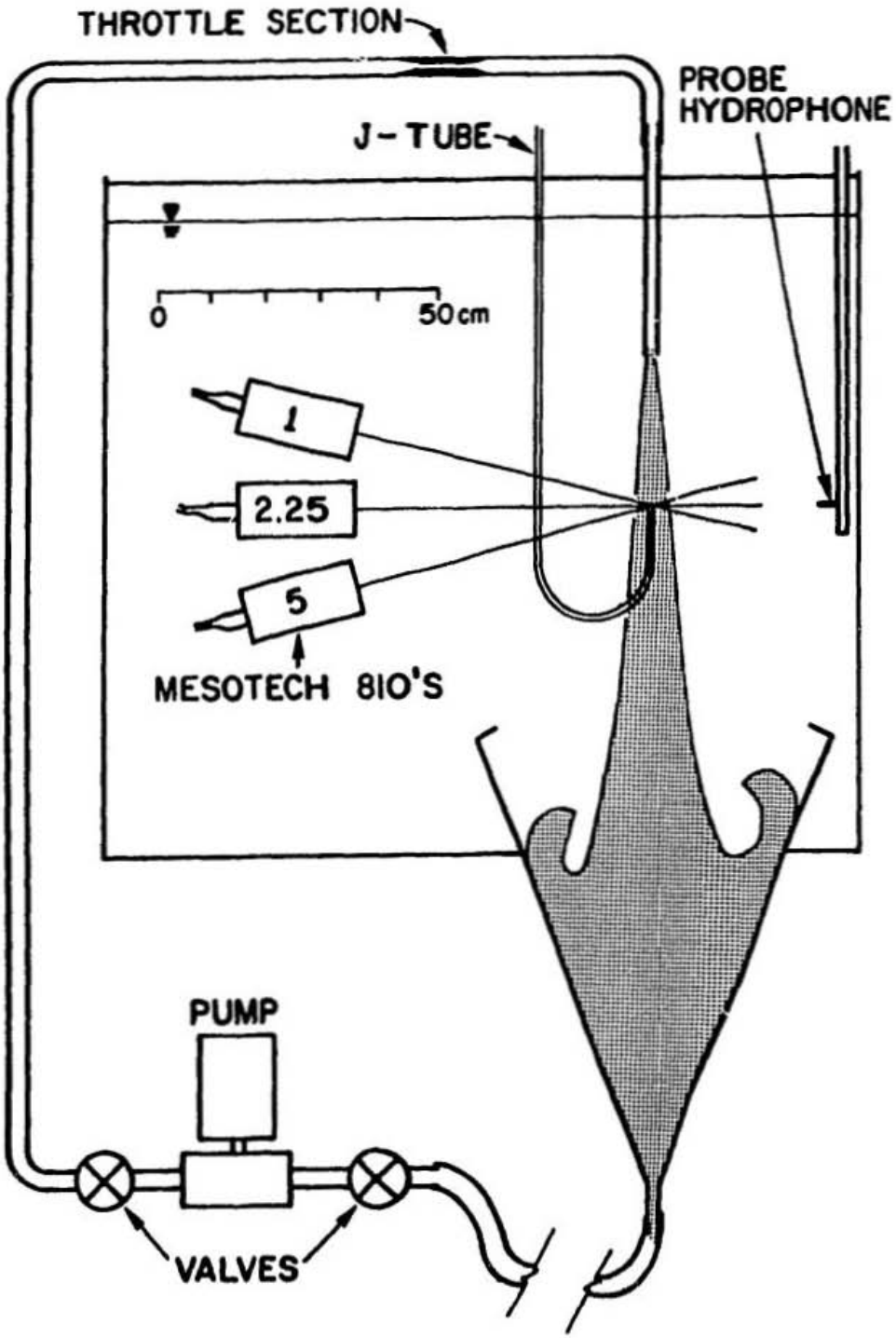

Figure 2.2: Configuration of laboratory tank setup, side-on [from Hay, 1991].

by a throttling section in the hose line. Sand suspended in the jet is collected in a large cone at the bottom of the tank. A lip at the cone edge deflects the excess flow due to entrainment by the jet inward so that sand loss from the recirculating system is minimized. The flow velocity through the hose is high enough that, except for the largest particles (425-500 μm in diameter), settling does not occur there. The nozzle is 2.0 cm in diameter, with a typical measured discharge velocity of 93 cm/s [Hay, 1991]. The Reynold's number in this case is 1.8×10^4, large enough that the flow is fully turbulent throughout the hose and jet.

The J-tube shown in Figure 2.2 was used for sampling suspended sediment concentration, and is moved well away from the jet when acoustic measurements are being made. Suction through the tube is driven by gravity at typical velocities of 150 cm/s [Hay, 1991]. Crickmore and Aked [1975] have outlined requirements for proper sampling using this method: flow velocity in the suction tube greater than the particle settling velocity (about 8 cm/s for 500 μm diameter grains), greater than the jet velocity (about 40 cm/s at the measuring point), and the intake directed into the flow. In the experiments reported here, four approximately 1 litre samples were collected for each measurement, and the standard deviation in the concentration determined from the four samples ranged between 0.4% and 13%, 5-7% being

typical. This gave a standard error for the suction measurements of concentration of 3% [Hay, 1991].

Properties of particles used in the laboratory experiments (density, compressional and shear wave velocities) are shown in Table 2.1. Lead-glass beads are a useful calibration tool, as they have been studied extensively [Hay and Schaafsma, 1989] and have well known properties. The sand used was from three experimental locations: Bluewater Beach, Ontario; Stanhope Beach, Prince Edward Island; and Queensland Beach, Nova Scotia. Sand grains from these three locations consist mostly of quartz, and physical properties of pure quartz, as listed in Table 2.1, have been used in calculations. Size fractions were separated into 1/4-phi intervals by sieving, according to the procedures described by Carver [1971]. On the logarithmic phi-scale, particle diameter in mm is given by 2^{-phi} . Sieve size fractions, median diameter and non-dimensional median radius for each fraction are listed in Table 2.2.

The size spectral density $n(a)$ for natural sand has been assumed to be log-normal [Sheng and Hay, 1991], i.e.

$$n(\ln a) = \frac{1}{\sqrt{2\pi}\ln\sigma_g}\exp\left(\frac{-(\ln a - \ln a_g)^2}{2\ln^2\sigma_g}\right) \qquad (2.1)$$

where a_g is the geometric mean radius and $\ln^2\sigma_g$ is the variance of $\ln a$.

Material	ρ_o' [kg/m^3]	c_c' [m/s]	c_s' [m/s]
Quartz	2650	5100	3200
Lead-Glass	2870	2940*	4800*
Water	1000	1482**	--

Table 2.1: Physical properties of particles at 20°C. * From measured travel times of compressional or shear waves at 2.25 MHz [Hay and Schaafsma, 1989]. ** Sound speed in water was calculated for a salinity S = 0 ppt using the relation given by Clay and Medwin [1977, p. 3].

Size Fraction	$\bar{d}$	$X = k_c\bar{a}$		
[$\times 10^{-6}$m]	[$\times 10^{-6}$m]	1 MHz	2.25 MHz	5 MHz
90.0 – 106.0	98.0	0.21	0.47	1.04
106.0 – 125.0	115.5	0.24	0.55	1.22
125.0 – 150.0	137.5	0.29	0.66	1.46
150.0 – 180.0	165.0	0.35	0.79	1.75
180.0 – 212.0	196.0	0.42	0.94	2.08
212.0 – 250.0	231.0	0.49	1.10	2.45
250.0 – 300.0	275.0	0.58	1.31	2.92
300.0 – 355.0	327.5	0.69	1.56	3.47
355.0 – 425.0	390.0	0.83	1.86	4.13
425.0 – 500.0	462.5	0.98	2.21	4.90

Table 2.2: Size fractions at 1/4-phi intervals. Sound speed in water is 1482 m/s (Temperature = 20°C, Salinity = 0 ppt). $\bar{d}$ and $\bar{a}$ represent the particle diameter and radius at the mid-point of the sieve intervals.

Natural (unsieved) sand types from the three locations mentioned above were used in the laboratory experiments. Characteristics of these sand types are listed in Table 2.3. d_{50} is the median diameter by weight and d_{16} and d_{84} are the diameters of the 16th and 84th percentile in the cumulative size distribution. Sets of experiments with each type of sand involved increasing the concentration between runs by adding more sand to the jet. For the

Location	d_{50} (μm)	d_{16} (μm)	d_{84} (μm)	σ_g
Bluewater Beach (BWB)	139	111	171	1.30
Stanhope Beach (PEI)	157	129	189	1.25
Queensland Beach (QLB)	360	275	460	1.35

Table 2.3: Size distribution parameters for natural sand from the locations listed.

experiments using narrow (1/4-phi) size fractions, measurements were made at a single concentration and all sand was removed from the recirculating system between runs.

2.2 Field Deployment and Experiments

The field data were collected at Stanhope Lane Beach, Prince Edward Island, during October and November 1989, during a collaborative experiment with groups from Dalhousie University and the University of Toronto. The deployment of the "wet" side of RASTRAN in the nearshore zone is shown in Figures 2.3 and 2.4. RASTRAN was positioned 200 m offshore in a mean water depth of approximately 2.2 m.

Raw samples incoming to the system were 4-ping ensemble-averaged, then 5 adjacent sample points were averaged so that there were 20 samples per stored data point. The 4-ping averaged profile acquisition rate was approximately 6.6 Hz with a range resolution of about 1.8 cm. Raw

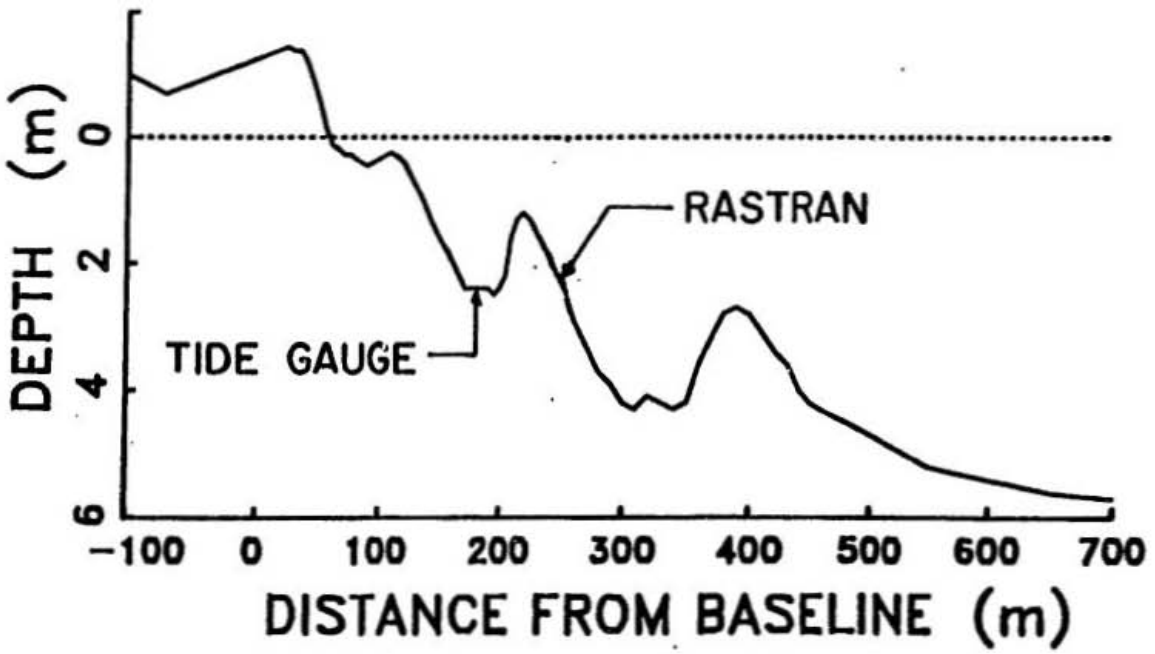

Figure 2.3: RASTRAN nearshore field deployment: profile of the beach topography at Stanhope Lane Beach [from Sheng and Hay, 1991].

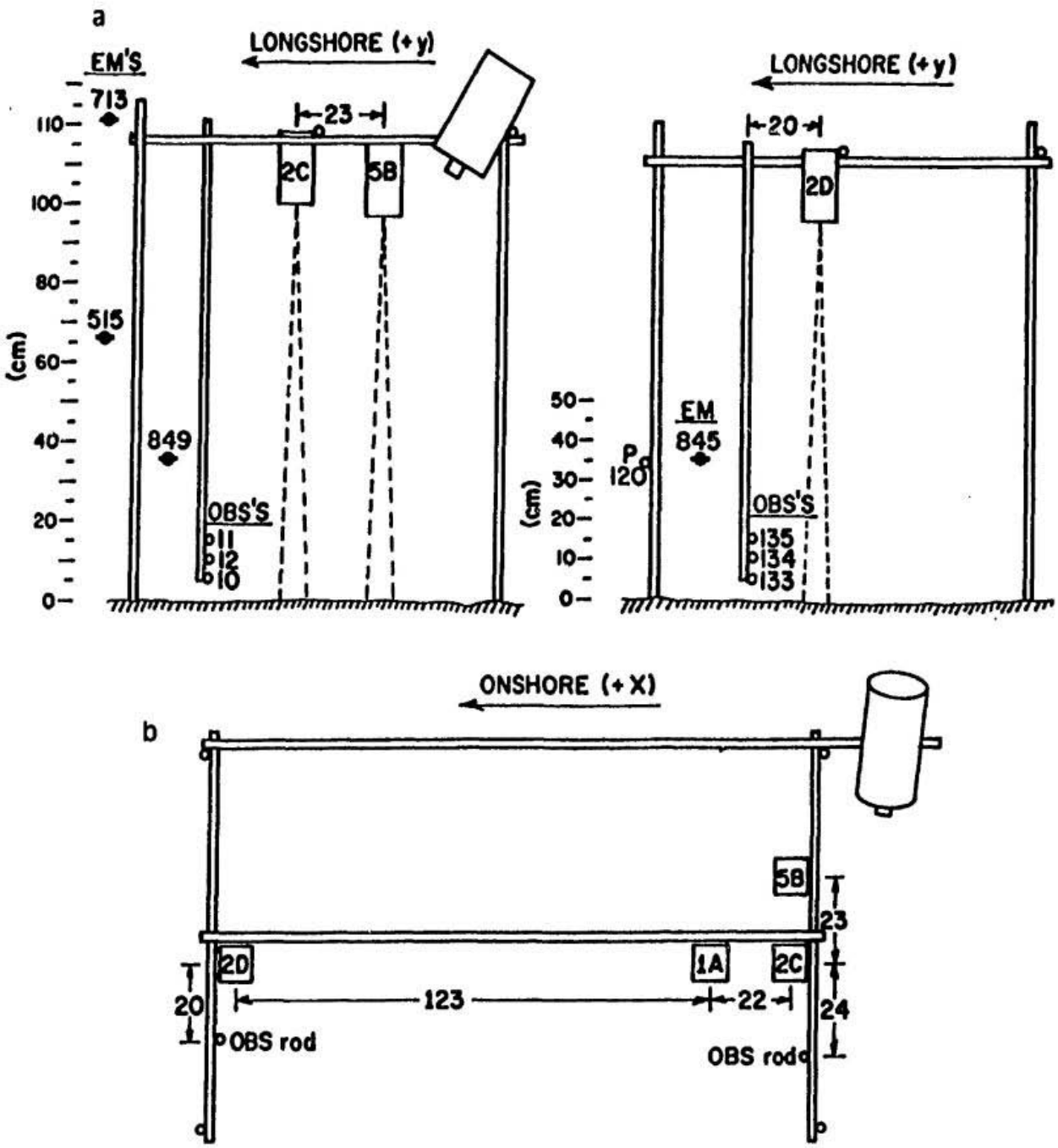

Figure 2.4: RASTRAN nearshore field deployment. Side views (a) and plan view (b) of the sensor array [from Sheng and Hay, 1991].

backscatter voltage data files containing 2600 4-ping averaged profiles were acquired over approximately 6.5 minute intervals.

At Stanhope Lane, four transducers operating at three frequencies were mounted, along with various other sensors, on a frame anchored to the seabed (Figure 2.4). Optical backscatter data were collected simultaneously by six Optical Backscatter Sensors, three at each end. Each array was set to monitor concentration at nominal heights of 5, 10 and 15 cm above the bottom. Six electromagnetic flowmeters were deployed as two sets of three, one group at each end of the frame, at heights of 20, 50 and 100 cm. A pressure sensor was also included on the shoreward end of the frame. The heights above bottom of the sensors are only approximate due to movement of the seabed. OBS, current meter and pressure data were logged by the Dalhousie University UDATS system [Hazen *et al.*, 1987] for 1/2-hour periods, usually overlapping 4 RASTRAN runs. OBS data from sensors 10, 11 and 12 are not available due to failure of a connector, so concentration level comparisons are made here using the OBS133 data, separated by 1.4 m from the 3-frequency transducer cluster.

Data to be presented here are taken from 5 sets of runs on 3 different days, as listed in Table 2.4. Conditions on these days were such that the data sets can be separated into categories by relative wave energy; high (H),

intermediate (I) and low (L) [Sheng, 1990].

Run number	$U_{1/3}$ (m/s)	T_p (s)
300.029–300.032 (L)	0.32	5.6
300.037–300.040 (L)	0.25	6.2
301.013–301.016 (I)	0.25	6.2
308.045–308.047 (H)	0.98	5.9

Table 2.4: RASTRAN data files selected for comparisons. *Run number* is Julian day followed by the consecutive number of the run during that day. $U_{1/3}$ is the significant wave orbital velocity, and T_p is the wave period at the main peak in the energy spectrum.

Chapter 3

Acoustic Backscattering Theory

The following section contains a brief discussion of the theory of acoustic scattering with reference to the specific case of backscatter from a collection of particles. More detailed versions of this treatment can be found in work by Sheng [1990] and Hay [1991], or in more general terms, in Morse and Ingaard [1968].

Consider a monostatic system, in which the same transducer is used both to transmit and receive. Such a system detects acoustic pressure which has been backscattered from objects in the path of the transmitted beam.

Assume that the scatterers are randomly and homogeneously distributed across the main lobe of the transducer beam pattern, and that there are many of them. Scattered waves returned to the transducer are assumed to be incoherent. A transmitted pulse of duration τ will define an outward moving volume, within which scatterers reflect some acoustic energy back toward the transducer. The geometry of the problem is shown in Figure 3.1.

Neglecting multiple scattering and assuming a freely moving, elastic, spherical scatterer, the incident pressure amplitude is given by

$$p_i = \frac{p_r r_r}{r} D \exp([i(k_c r - \omega t)] - \alpha_o r - \Delta) \tag{3.1}$$

where r is the radial distance from the center of the transducer face and $r \gg r_r$. p_r is a reference level for the on-axis pressure at distance r_r. D is the directivity of the transducer. The attenuation due to the ambient fluid, α_o, is considered to be constant over the range r, and depends on the salinity and temperature of the water [Clay and Medwin, 1977]. Δ is the integrated scattering attenuation, given by

$$\Delta = \int_0^r \alpha_s dr' \tag{3.2}$$

where α_s is the scattering attenuation coefficient, which will be discussed further in a later section, k_c is the compressional wave number in the ambient

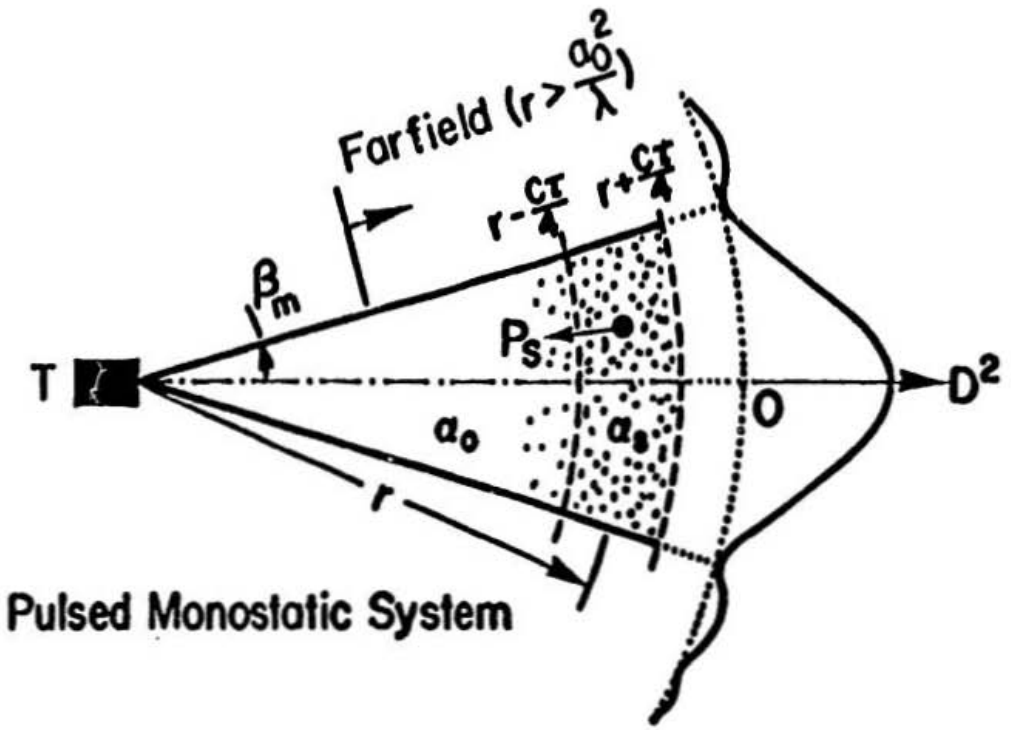

Figure 3.1: Backscattering geometry for a monostatic system [from Sheng, 1990].

fluid, and ω is the angular frequency. The factor $\exp[i(k_c r - \omega t)]$ will be dropped at this point for convenience.

The backscattered pressure amplitude from a single spherical particle is

$$p_s = p_i \frac{a|f_\infty(X)|}{2r} \exp(-\alpha_o r - \Delta) \tag{3.3}$$

where $X = k_c a$. Here, r is from the center of the scatterer. $f_\infty(X)$ is the far-field backscattering form factor. The acoustic far-field, in this case, is the region surrounding the scatterer where $k_c r \gg 1$ and $r > a$.

At the transducer, the backscatter from a collection of scatterers is the sum of the backscatter from each particle found in the detected volume. For a rectangular pulse of duration τ, the detected volume at range r_o is given by

$$V_d = \int_{r_o - \frac{c\tau}{4}}^{r_o + \frac{c\tau}{4}} \int_0^{2\pi} \int_0^{\beta_m} r^2 \sin\beta d\beta d\theta dr \tag{3.4}$$

where β_m is the angle to the first zero of D. There is virtually no contribution from the side lobes which are below -12 dB from the main lobe maximum [Sheng, 1990]. Beam pattern characteristics for the transducers used are listed in Table 3.1. Assuming uniform size and constant concentration for the scatterers in V_d, the mean square pressure backscattered detected by the transducer is given by

$$< p^2 >= p_r^2 r_r^2 \frac{|f_\infty(X)|^2 a^2}{4} \int_{r_o - \frac{c\tau}{4}}^{r_o + \frac{c\tau}{4}} \int_0^{2\pi} \int_0^{\beta_m} N D^4 \frac{e^{-4\alpha r}}{r^2} \sin\beta d\beta d\theta dr \tag{3.5}$$

Frcq. [MHz]	a_o [cm]	a_o^* [cm]	R_c [cm]	β_m [deg.]
1.00	1.09	1.27	25.2	4.75
2.25	0.47	0.64	10.6	4.87
5.00	0.24	0.32	6.1	4.39

Table 3.1: Properties of the tranducers. c = 1482 m/s, for T = 20°C, S = 0 ppt. β_o is the -3 dB width of the beam pattern. a_o is the radius of the transducer face and a_o^* is the *effective* radius, determined by fitting a theoretical beam pattern to measured values. $R_c = \pi a_o^*/\lambda$ is the far-field critical range.

The attenuation coefficient α includes attenuation due to the ambient fluid and scattering attenuation —

$$\alpha = \alpha_o + \frac{\Delta}{r} \tag{3.6}$$

Thermal attenuation [Hay and Burling, 1982] and viscous effects [Hay and Mercer, 1985] can be neglected for quartz particles in the sand size range in laboratory and field experiments. If the number density of scatterers, N, is independent of β and θ, and $r_o \gg \frac{c\tau}{4}$, Equation 3.5 can be written as [Hay, 1991]

$$< p^2 >= P_r^2 r_r^2 \frac{|f_\infty|^2 a^2}{4} \left[2\pi \int_0^{\beta_m} D^4 \sin\beta d\beta\right] \frac{\exp[-4\alpha_o r_o - 4\Delta_o]}{r_o^2} \left[\frac{c\tau}{2} N(r_o) \frac{\sinh[(\alpha_o + \alpha_{so})c\tau]}{(\alpha_o + \alpha_{so})c\tau}\right] \tag{3.7}$$

where α_{so}, Δ_o, and $N(r_o)$ refer to values at range r_o. Substituting

$$A = 4\Delta_o = 4\int_0^{r_o} \alpha_s dr \tag{3.8}$$

and

$$B = (\alpha_o + \alpha_{so})c\tau \tag{3.9}$$

Equation 3.7 becomes

$$< p^2 >= p_\tau^2 r_\tau^2 \frac{|f_\infty|^2 a^2}{4} \left[2\pi \int_0^{\beta_m} D^4 \sin\beta d\beta \right] \frac{\exp[-4\alpha_o r_o]}{r_o^2} \frac{c\tau}{2} N(r_o) e^{-A} \frac{\sinh B}{B} \quad . \tag{3.10}$$

Note that this applies to the case where N is uniform over the detected volume. This may not always be valid, as will be discussed later.

The voltage output from the transducer (v) for a given input mean squared pressure depends on a system sensitivity constant, S_N —

$$< v^2 >= S_N^2 |f_\infty|^2 a^2 \frac{c\tau}{2} N(r_o) e^{-A} \frac{\sinh B}{B} \tag{3.11}$$

This constant factor is determined empirically. Note that the factor $e^{-4\alpha_o r_o}/r_o^2$ has been dropped from the expression — the voltage output from the transducers in this application is corrected for this attenuation and spreading loss factor by Time-Variable Gain (TVG) amplification in the receiver.

Assuming spherical scatterers with density ρ_o', then

$$N = \frac{M}{\frac{4\pi}{3} a^3 \rho_o'} \tag{3.12}$$

where M is the mass concentration of scatterers. Using this relation, Equa-

tion 3.11 can be rewritten as

$$< v^2 >= S_M^2 \frac{|f_\infty|^2}{a} \frac{c\tau}{2} \frac{M(r_o)}{\rho_o'} e^{-A} \frac{\sinh B}{B} \tag{3.13}$$

where the relation $S_M^2 = 3S_N^2/4\pi$ has been used. Assumptions made in the derivation of Equation 3.13 are not limiting in most cases. Sheng and Hay [1988] determined that the single scattering assumption is valid for scatterer concentrations typically found in laboratory and most field experiments. This is supported by more rigorous treatment by Varadan *et al.* [1983]. Hay [1991] found that laboratory measured scattering attenuation is linear with concentration up to 30 g/l, verifying that multiple scattering is not significant over this range of concentrations. As will be seen, inhomogeneity of scatterer distribution within the detected volume can be a factor in regions of high concentration gradient.

Equation 3.13 is the basic equation relating the size and concentration of scatterers to measured voltage. Estimates of concentration and size can be obtained from $< v^2 >$ only after the calibration factor S_M has been determined and the frequency/size dependence of the backscattering form factor is known. The calibration procedure has been described by Hay [1991], and is similar to the general laboratory techniques described in Section 2.1. Backscatter measurements are made from glass beads of various

sizes suspended in the jet. For concentrations of scatterers small enough that $A, B \sim 0$, Equation 3.13 can be written as

$$< v^2 >^{1/2} \kappa = \frac{|f_{\infty g}(X)| M_o}{X} \tag{3.14}$$

where $X = k_c a$, M_o is the measured centerline concentration, $|f_{\infty g}|$ is the backscattering form factor for lead-glass beads in water and

$$\kappa = \frac{1}{S_M} \left[\frac{2\rho_o'}{k_c c \tau} \right]^{1/2} \tag{3.15}$$

Previous work [Hay and Schaafsma, 1989] has shown that the theoretical form factor, $|f_{\infty g}|$, fits experimental data for the total scattering cross section, and glass beads in suspension as standard targets have been used to obtain system sensitivity constants, S_M. Everything in Equation 3.14 is known except S_M. Results of calibration experiments performed by Hay [1991] are listed in Table 3.2. S_M is determined by least-squares fit of the values determined from Equations 3.14 and 3.15.

Transducer	S_M^2 [V^2]
1.00A	1.588
2.25C	0.413
5.00B	0.054

Table 3.2: System sensitivity constants for the three transducers, labelled by frequency in MHz and identification letter.

3.1 The Acoustic Backscattering Form Factor — $|f_\infty(X)|$

The backscatter form factor for natural sand has been studied in detail by others [Hay and Mercer, 1985; Sheng, 1986; Hay and Schaafsma, 1989], and results of these studies have been used in this work. The scattered pressure from a solid elastic sphere can be written

$$p_s = \frac{p_o a}{2r}\left[\frac{2}{X}\sum_{n=0}^{\infty}(2n+1)(-iA_n)P_n(\cos\theta)\right]\exp[ik_c r]$$
$$= \frac{p_o a}{2r} f_\infty(\theta, a)\exp[ik_c r] \qquad (3.16)$$

so that

$$f_\infty(\theta, a) = -\frac{2}{k_c a}\sum_{n=0}^{\infty}(2n+1)iA_n P_n(\cos\theta) \qquad (3.17)$$

The $P_n(\cos\theta)$ are Legendre polynomials and θ is the scattering angle. The quantity $|f_\infty| = (f_\infty f_\infty^*)^{1/2}$, where * denotes the complex conjugate, relates the amplitudes of the incident and scattered pressure waves. For the case of backscattering, $\theta = \pi$. The complex amplitude coefficients, A_n, are often written in terms of η_n, the phase shift of the nth partial wave [Hay and Mercer, 1985], such that

$$iA_n = \sin\eta_n \exp[-i\eta_n] = \frac{\tan\eta_n}{1 + i\tan\eta_n} \qquad (3.18)$$

The phase shifts are given by [Faran, 1951]

$$\tan \eta_n = \tan \delta_n(X) \frac{\tan \alpha_n(X) + \tan \Phi_n(X', s')}{\tan \beta_n(X) + \tan \Phi_n(X', s')} \tag{3.19}$$

where

$$\tan \Phi_n = \frac{\frac{\rho_o s'^2}{2\rho_o'} \left[\frac{\tan \alpha_n(X')}{\tan \alpha_n(x')+1} - \frac{n^2+n}{(n^2+n-1)-s'^2/2+\tan \alpha_n(s')} \right]}{\left[\frac{n^2+n-s'^2/2+2\tan \alpha_n(X')}{\tan \alpha_n(X')+1} - \frac{(n^2+n)(\tan \alpha_n(s')+1)}{(n^2+n-1)-s'^2/2+\tan \alpha_n(s')} \right]} \tag{3.20}$$

The terms $\tan \alpha_n$, $\tan \beta_n$ and $\tan \delta_n$ are ratios of spherical Bessel functions. $X' = k_c' a$, $s' = k_s' a$ and $X = k_c a$, where k_c' and k_s' are the compressional and shear wavenumbers in the scatterer. Physical properties of the scatterers enter Equation 3.17 through the $\tan \Phi_n$ term in Equation 3.19.

Sheng [1990] proposed that the theoretical result for spherical quartz particles could be modified to fit experimental form factor data for natural sand grains. Figure 3.2 shows measured values for $|f_\infty|$ for sand, taken from experiments performed in the suspended sediment jet [Hay, 1991]. The short-dashed line in Figure 3.2 is the theoretical form factor for a rigid, movable scatterer, while the medium-dashed line is Sheng's semi-empirical result. The semi-empirical form factor which has been introduced is based on the theoretical result, with smoothing and stretching —

$$|f_{\infty s}|^2 = \frac{(1 + 1.25X^4)^2}{(1 + X^4)^2} \left[\frac{a \int_0^\infty a^2 |f_\infty|^2 n(a) da}{\int_0^\infty a^3 n(a) da} \right] \tag{3.21}$$

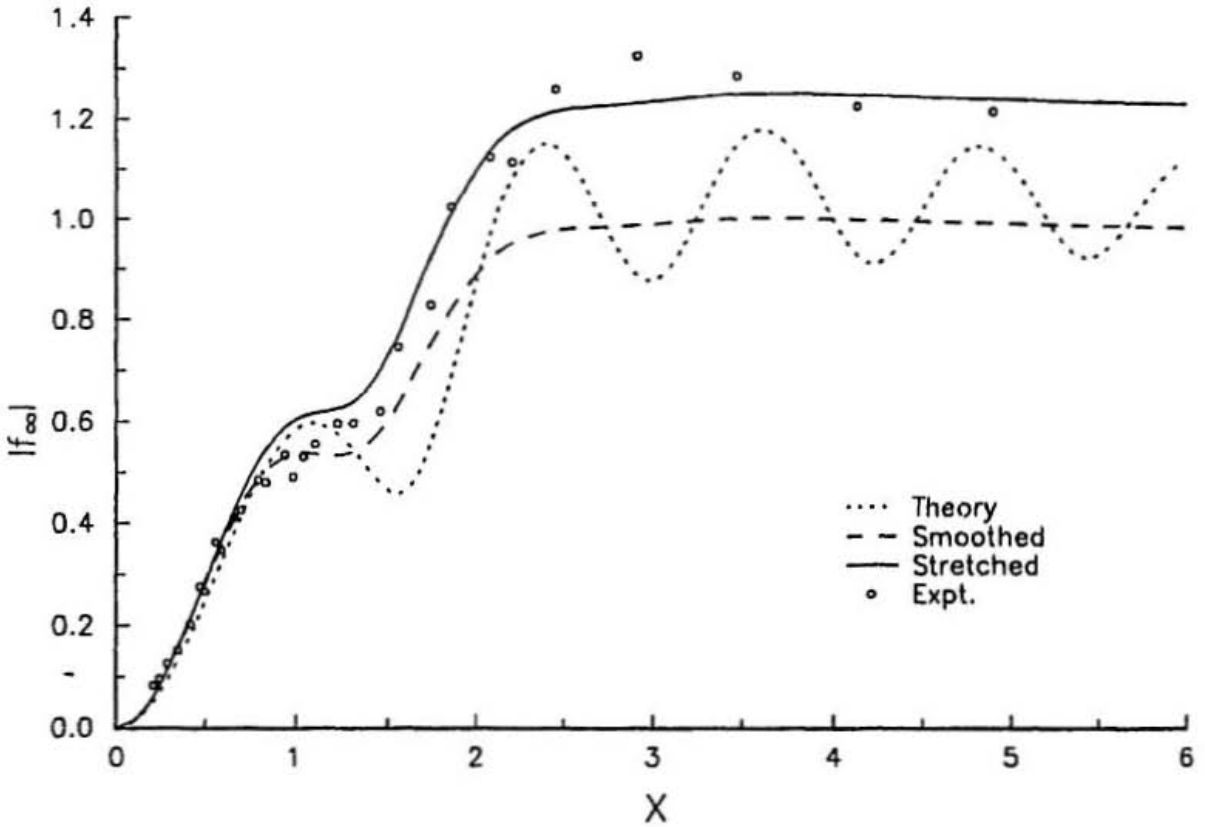

Figure 3.2: Backscatter form factor, $|f_\infty|$, for natural sand grains in water. Short-dashed line is theory for rigid, mobile scatterers, medium-dashed line is smoothed and solid line is smoothed and stretched. Data (o) are from laboratory measurements.

where $n(a)$ is the distribution function for size. In this case, Sheng assumed a log-normal distribution for n, with $\sigma_g = 1.2$. The term in square brackets smooths the form factor (as shown by the solid line in the Figure), while the leading term is a vertical stretching coefficient. The oscillations evident in the purely theoretical form factor for spherical particles are not seen in the experimental data, which were collected from backscatter experiments using irregularly shaped natural sand particles. $|f_{\infty s}|$ is smooth and, for $X > 1$, the stretching term has corrected the offset between the measured data and theory.

Sheng's semi-empirical form factor does not, in fact, fit the measured data very well for $X > 0.75$. An alternative approach is to obtain a better fit to the experimental data by using a rational fraction fit [Hornbeck, 1975], as suggested by Lewis [personal communication from Dr. J. Lewis, Memorial University of Nfld.]. After some experimentation, a reasonable fit was accomplished using the approximation

$$|f_{\infty r}(X)| = \frac{0.6 + 1.33\left[\frac{X}{1.91}\right]^{10}}{1 + \left[\frac{X}{1.91}\right]^{10}} \times \frac{0.4X + \left[\frac{X}{0.6}\right]^{3}}{1 + \left[\frac{X}{0.6}\right]^{3}} \times \frac{1 + 0.91\left[\frac{X}{3.7}\right]^{16}}{1 + \left[\frac{X}{3.7}\right]^{16}} \quad (3.22)$$

This is shown in Figure 3.3, plotted with the same experimental data as in Figure 3.2, and the semi-empirical form factor (dashed line). The error associated with the experimental values shown in Figure 3.3 is approximately

±5% so that both curves fall within the error limits of the data. The rational fraction fit follows the data much more closely in the $X \sim 1$ region. The percentage difference between the two approximations to the measured form factor is shown in Figure 3.4. The most notable difference is in the region $0.5 < X < 2$. Referring to Table 2.2, it can be seen that this range of X values includes sizes larger than about 230 μm for 1 MHz, between about 100 and 400 μm for 2.25 MHz, and up to 190 μm for 5 MHz - i.e. this difference will have an effect on determining size over much of the size range of interest. The large difference in the range $X < 0.3$ effects sizes below about 140 μm in the 1 MHz case only. Calculation using both expressions for the form factor are presented later. Also shown in Figure 3.3 is the small X limit dependence of the form factor. If the acoustic wavelength is much greater than the particle radius, i.e. in the Raleigh scattering limit, pressure scattered from a compressible sphere which is free to move can be written [eg. Hay, 1983]

$$p_s = p_i \frac{k_c^2 a^3}{3r}(\gamma_\kappa + \gamma_\rho \cos\theta)\exp[i(k_c r - \omega t)] \tag{3.23}$$

where

$$\gamma_\kappa = \frac{\kappa_s' - \kappa}{\kappa} \tag{3.24}$$

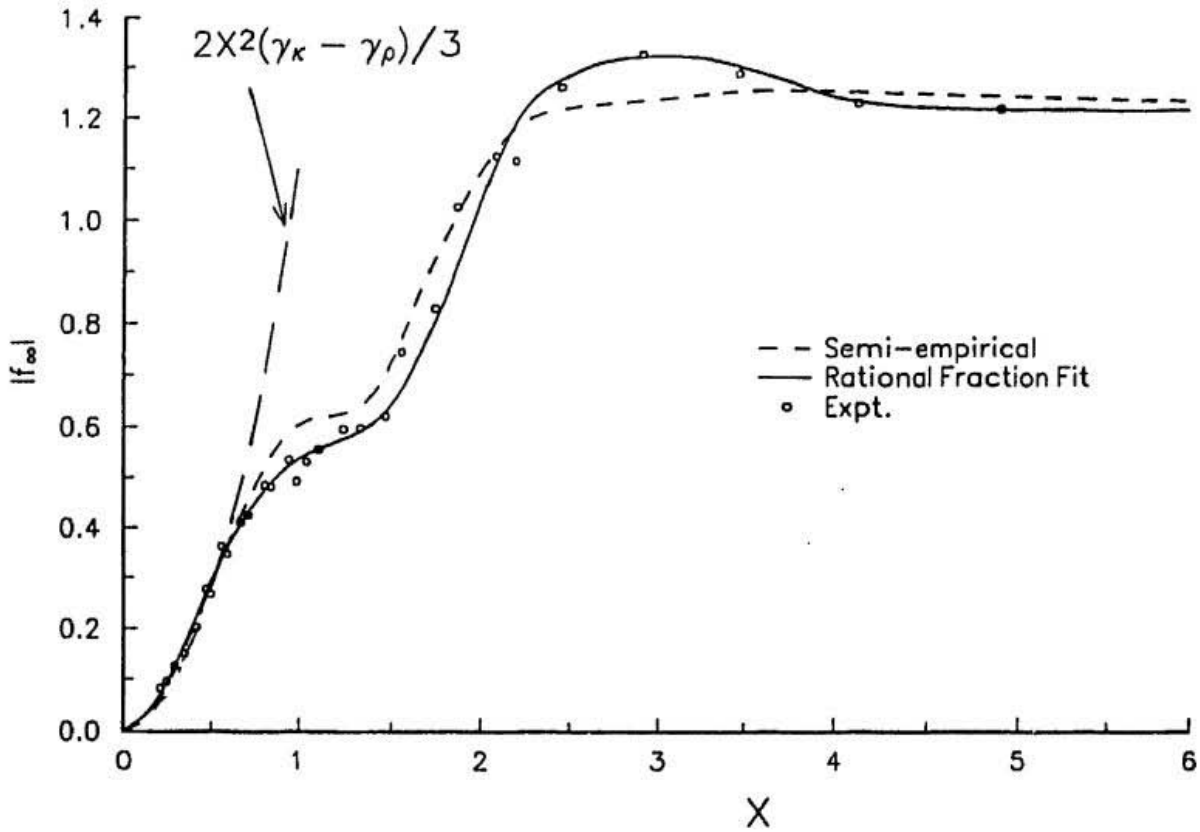

Figure 3.3: Rational fraction fit (solid line) to experimental backscattering form factor data. The semi-empirical form factor (dashed line) and measured data (o) are also shown for comparison Also shown is the small X limit dependence, given by the inset equation.

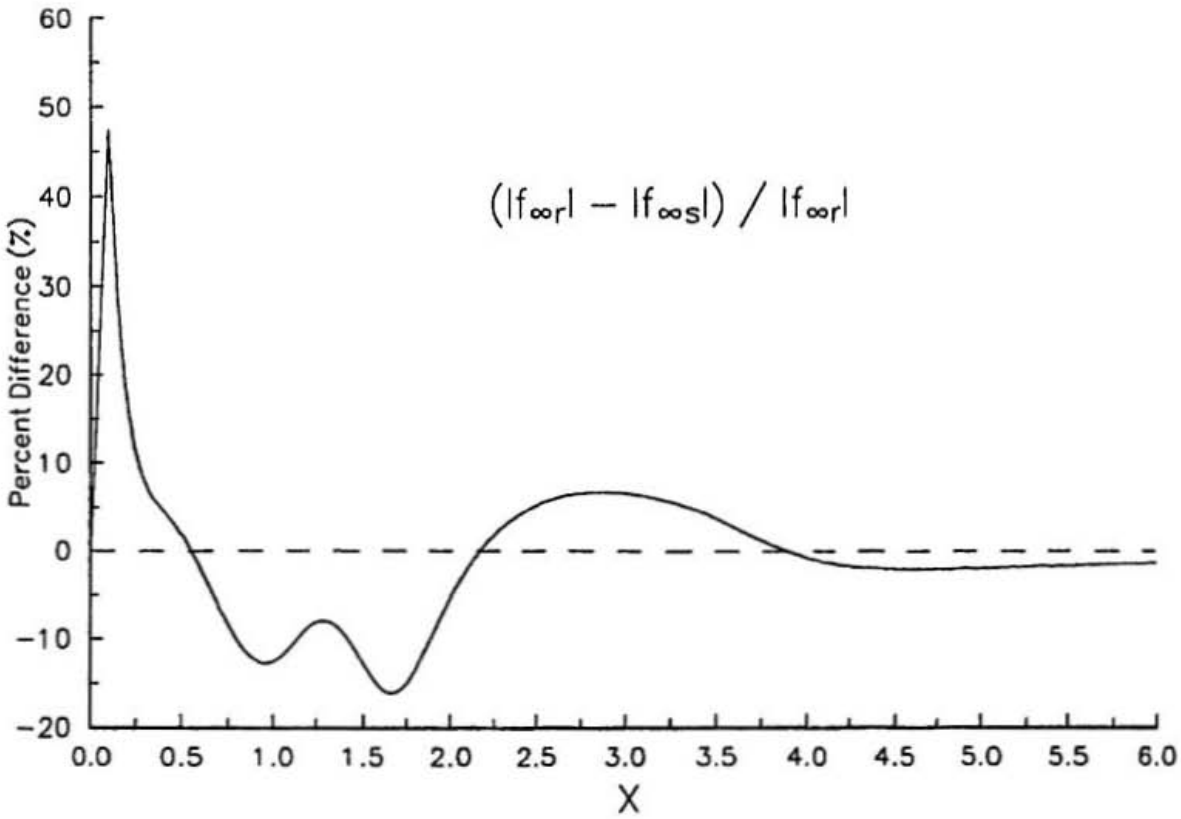

Figure 3.4: Percentage difference between the semi-empirical and rational fraction fit form factors — $(|f_{\infty r}| - |f_{\infty s}|)/|f_{\infty r}|$, where $|f_{\infty r}|$ is the rational fraction fit approximation and $|f_{\infty s}|$ is the semi–empirical expression.

and

$$\gamma_\rho = \frac{3(\rho_o' - \rho_o)}{2\rho_o' + \rho_o} \tag{3.25}$$

κ is the bulk compressibility, which for a solid, is given by $\kappa_*' = [\lambda' + 2\mu'/3]^{-1}$ where λ' and μ' are the Lamé constants. For quartz in water, $\gamma_\kappa = -0.93$ and $\gamma_\rho = 0.77$. In the Raleigh limit, individual features of the scatterer, which are necessarily smaller than the radius, become insignificant so that irregularly shaped particles appear as spheres [Raleigh, 1945]. Comparing Equations 3.3 and 3.23, the small X behavior of $|f_\infty|$ can be seen to be given by

$$|f_\infty| \sim \frac{2X^2(\gamma_\kappa - \gamma_\rho)}{3} \tag{3.26}$$

Both approximations to the form factor data follow this dependence closely for $X < 0.5$, however, both fall slightly above this limiting function. The rational fraction fit has nearly linear dependence on X in this region, as seen in Equation 3.22.

3.2 Scattering Attenuation Correction

Particles suspended in fluid contribute to the attenuation of acoustic energy. This effect obviously depends on the concentration of scatterers, but also depends on the size of the individual particles.

The total scattering cross section is given by Morse and Ingard [1968, p. 427] as

$$\Sigma_s = \frac{2\pi a}{k_c}\mathrm{Im}[f_\infty(\theta = 0)] \tag{3.27}$$

For a collection of uniformly-sized spherical particles, the pressure attenuation coefficient due to scattering is then given by

$$\alpha_s = \frac{N\Sigma_s}{2} \tag{3.28}$$

It is logical that the scattering attenuation depends on the scattering form factor. Sheng and Hay [1988], however, determined that a modified form of the simple "high-pass model" for backscattering intensity proposed by Johnson [1977] leads to a suitable approximation for scattering attenuation. Using this idea,

$$\frac{a\alpha_s}{\epsilon} = \frac{\kappa_\alpha X^4}{[1 + \frac{4}{3}\kappa_\alpha X^4 + \xi X^2]} \tag{3.29}$$

where

$$\kappa_\alpha = \frac{\gamma_\kappa^2 + \gamma_\rho^2/3}{6} \tag{3.30}$$

and $\epsilon = M/\rho_o'$ is the volume concentration of scatterers. ξ is an adjustable constant, set to 1 in this application, and for quartz in water, $\kappa_\alpha = 0.18$.

Measurements of scattering attenuation were obtained using a probe hydrophone located opposite the jet from the 2.25 MHz transducer unit at

range r_H (shown in Figure 2.2). Voltage output from the hydrophone is given by

$$v_H(M_o) = \frac{v_o}{r_H} e^{(-\alpha_o r_H - A/2)} \tag{3.31}$$

where v_o is a constant, M_o is the measured centreline sand concentration and $A/2$ is the attenuation due to particles across the full width of the jet. $A/2$ is determined by comparing v_H with the jet off ($v_H(0)$) and with the jet on and carrying sand —

$$\frac{A}{2} = \ln\left[\frac{v_H(0)}{v_H(M_o)}\right] \tag{3.32}$$

Comparison of measured and calculated values of $A/2$ will be presented later.

3.3 The Geometric Correction Factor — F

Equation 3.10 carried the disclaimer that in some cases the mean concentration of scatterers may not be uniform across the detected volume. In such cases, a correction factor F must be applied. F has not been included in calculations presented here — it has been assumed that $F \sim 1$. A more detailed description of F for the jet scattering experiments is given by Hay [1991].

Referring to Equation 3.7, the departures from homogeneity in the mean N between $r_o + c\tau/4$ and $r_o - c\tau/4$ can be accounted for by multiplying by the ratio

$$F = \frac{\int_{r_o-c\tau/4}^{r_o+c\tau/4} \int_0^{2\pi} \int_0^{\beta_m} N D^4 r^{-2} \exp[-4\alpha_o r - 4\Delta] \sin\beta d\beta d\theta dr}{2\pi \left[\int_0^{\beta_m} D^4 \sin\beta d\beta\right] r_o^{-2} \exp[-4\alpha_o r_o] \frac{c\tau}{2} N(r_o) e^{-A} \frac{\sinh B}{B}} \qquad (3.33)$$

When N is independent of r, θ and β within the detected volume, then the numerator becomes equal to the denominator. Note that Equation 3.33 has been formulated to apply to a gradient in the *mean* number density profile, not including concentration fluctuations superimposed on that mean. The effect of these fluctuations on F has not been examined. An analytical expression for F at the centreline of the jet has been developed and computed [Hay, 1991]. The value of F in this case varies from about 0.8 for $M_o \sim 0$ g/l to about 1.3 for $M_o \sim 30$ g/l, crossing 1 at about 10 g/l.

Chapter 4

Inversion Algorithm

The basis of this inversion approach is the difference between backscatter amplitude at different operating frequencies. A previously developed algorithm (Sheng [1990], Sheng and Hay [1991]) uses ratios of signal levels. Both methods involve determination of an average scatterer size, and then use this estimate in calculating a mean concentration. Some pre–processing of the raw voltage data is required.

Raw RASTRAN data are stored in binary data files of a standard format. Header information includes the number of records, channels and range bins per record, as well as system configuration information. Entries in the data file represent pre-averaged rectifier output voltage in mV. Each record in the

binary file contains a multifrequency profile, called a *set* which represents the ensemble-average of the backscatter profiles from a number of consecutive pings. A set is divided into channels for each transducer unit (operating at the individual frequencies), and further subdivided into the single entries (*bins*) representing range increments.

These raw data must go through several pre-processing steps before use in the inversion algorithm. In cases where the transducers have been deployed at different levels above the bottom, the height discrepancy between channels must be corrected. Optimally, the transducers monitor the same detected volume. In practice, this is not possible. Channels corresponding to transducers located farther from or closer to the bottom, or to the center of the jet, are numerically shifted by an integral number of range bins. When Time-Variable Gain corrections are later applied to this shifted data (see below), this range adjustment is taken into account.

Background voltage levels are determined from "quiet" periods in the run, identified by visual examination of the raw data displayed using imaging software previously developed for use with RASTRAN data. Once a period of low suspensate concentration has been identified, a background level profile is compiled by averaging the sets in this time range. The background value for each bin is subtracted directly from the raw voltage before

any other calculation is done.

Output from the Mesotech 810 transducers has already been TVG (Time-Variable Gain) corrected for attenuation in water and spherical spreading (the $e^{-4\alpha_w r_o}/r_o^2$ term in Equation 3.10). However, the attenuation and sound speed used in this correction are factory set. In most cases, the ambient values differ from these settings, and the output voltage must be recorrected. System dependent factors, such as the rectifier threshold and gain settings, must also be applied.

Equation 3.13 relates the mean concentration and size for a particular range bin to $< v^2 >$. Once the raw voltage has been corrected, it is squared, then averaged over a specified number of sets. Averaging is an important aspect of the signal processing, and will be discussed in relation to this application later.

A flow chart of the inversion algorithm is shown in Figure 4.1. The following is a description of the reasoning behind this scheme.

Equation 3.13 can be rearranged to form

$$\frac{< v^2 >}{S_M^2 |f_\infty(X)|^2} = \frac{c\tau}{2} \frac{M}{\rho_o' a} \tag{4.1}$$

where A, $B \sim 0$ for small concentrations of scatterers. Since the concentration and size of particles detected in a particular range bin should be

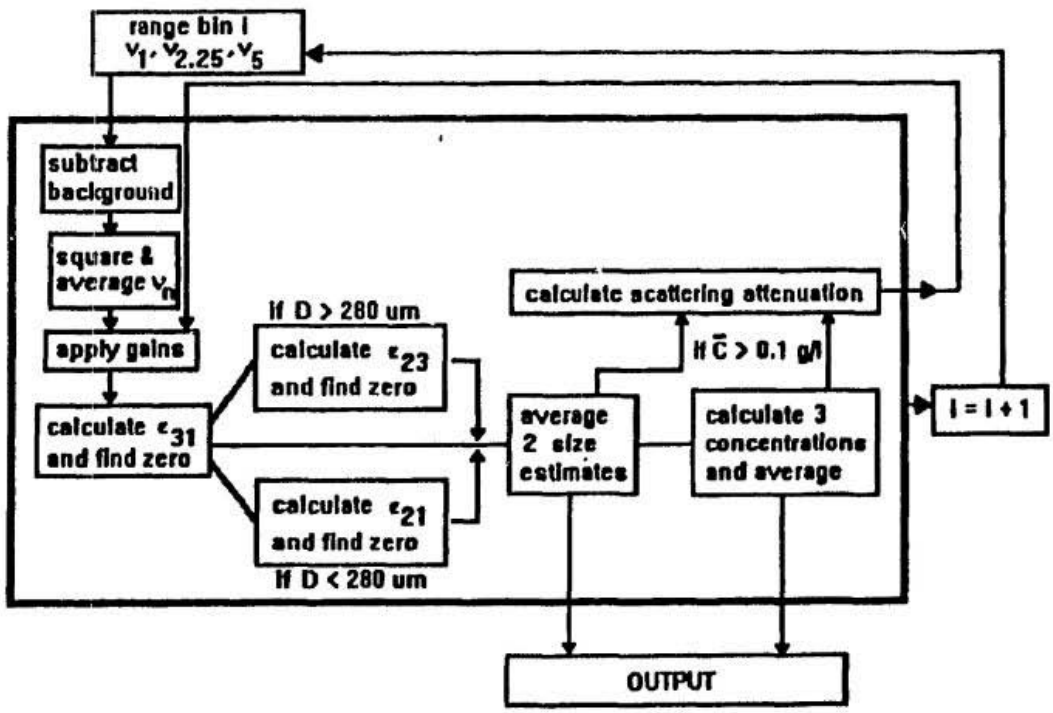

Figure 4.1: Flow chart of the inversion algorithm.

approximately the same for each channel, then the difference between the left-hand side of Equation 4.1 for different frequency pairs should be small. That is,

$$\frac{< v_m^2 >}{(S_M)_m^2 |f_{\infty m}(X_m)|^2} - \frac{< v_n^2 >}{(S_M)_n^2 |f_{\infty n}(X_n)|^2} = \epsilon_{mn} \qquad (4.2)$$

where ϵ_{mn} is small, and $m \neq n$, denote a pair of the three channels. $m, n =$ 1, 2 and 3 correspond to operating frequencies of 1, 2.25 and 5 MHz, respectively. The left side of Equation 4.2 is only dependent on a through $X_m = k_c a$.

When $\epsilon_{mn} \rightarrow 0$,

$$\frac{< v_m^2 >}{(S_M)_m^2 |f_{\infty m}(X_m)|^2} \simeq \frac{< v_n^2 >}{(S_M)_n^2 |f_{\infty n}(X_n)|^2} \ . \qquad (4.3)$$

The value of a for which this is true is an estimate of the mean size in that range bin. In practice, the final size estimate is an average of two zero–crossing locations, so that $|\epsilon_{mn}(a_{\text{final}})| > 0$. The difference in size estimates from the pairs of channels is due to statistical fluctuations or systematic error leading to discrepancies between the "size" seen by different channels. It has been assumed here that the size distribution of the particles in suspension has a single dominant size. If the peak in the distribution is ill–defined, or the distribution is bimodal, this inversion technique cannot return meaningful estimates. The naturally occurring distributions at the three locations of

field deployment are unimodal [Sheng, 1990], as is commonly the case with sandy beach sediments [Komar, 1976].

Figure 4.2 shows examples of ϵ_{mn} versus diameter from jet experiments. Average centreline voltages (over all 200 sets in each of the laboratory runs) for the three channels using 116 μm and 390 μm diameter sand were input to Equation 4.2 to calculate ϵ_{mn} with $D = 2a$ as an independent variable, as shown in Figures 4.2a and b. Observation of many such plots have shown that a good first estimate of size is given by $\epsilon_{31} = 0$. According to whether this estimated diameter is above or below 280 μm, the zero values of ϵ_{23} or ϵ_{21}, respectively, are used. Figures 4.2a and b illustrate these two cases. With increasing size, the zero crossing of ϵ_{21} follows the real size of the scatterers to an upper limit of $D \sim 300$ μm. Above this size, the zero crossing of ϵ_{23} is a better estimate. The multivalued behavior of ϵ_{23} for $D <$ 280 μm leads to ambiguity in the location of the root, as seen in Figure 4.2a. The average of the two resulting size estimates is carried forward as the mean size of scatterers in that range bin.

Once a mean size has been determined for a particular range bin, concentration is calculated using Equation 3.13 for each of the three frequencies. The average of these three estimates is the mean concentration for that bin.

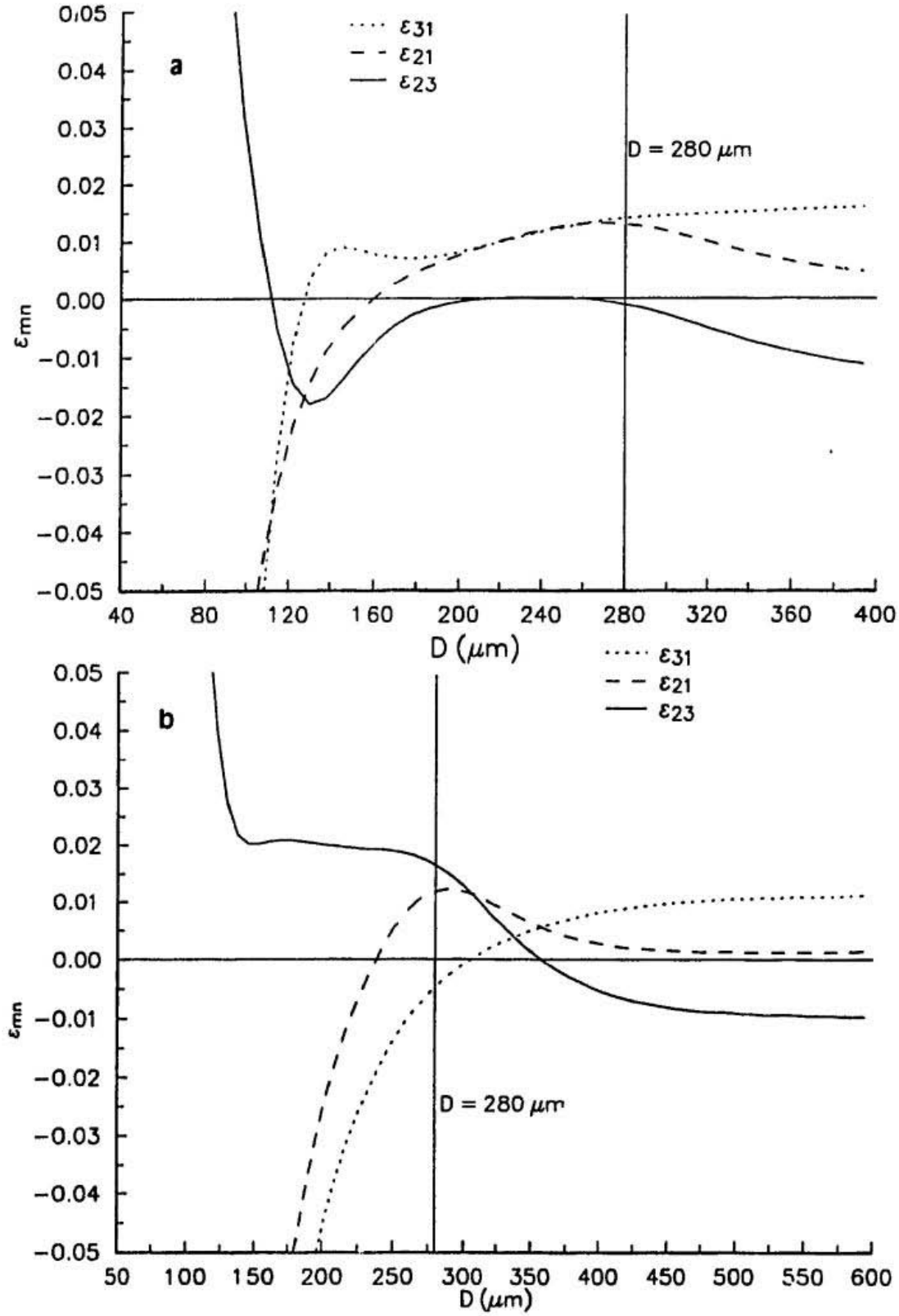

Figure 4.2: ϵ_{mn} versus diameter for large and small sizes. Calculated from experimental averaged centreline voltages for runs using sand of diameter 116 μm (a) and 390 μm (b).

4.1 Calculation of Scattering Attenuation

If the final estimate of mean concentration in a particular range bin is above a certain level (0.1 g/l, in this case), then this value is used to calculate scattering attenuation. The scattering attenuation correction factor incorporates Equation 3.29 in the term $e^{-A} \sinh B/B$, calculated from the current estimates of concentration and size. The reciprocal of this factor is applied as a gain to the raw voltage of the following bin. Scattering attenuation accumulates with range as regions containing concentrations greater than the threshold are crossed.

This correction term has been examined in detail, with comparison to laboratory measurements of attenuation made in conjunction with acoustic backscatter measurements. Results of this comparison will be discussed further in Section 5.2.

4.2 Comparison With an Earlier Inversion Scheme

Work done previously by Sheng [1990] has resulted in an earlier voltage-size and concentration inversion algorithm. His results have been presented [Sheng and Hay, 1991] and are quite good.

Sheng's approach is fundamentally different from the method outlined

above. Ratios of measured voltages are matched to pre-computed tables of theoretical values to extract the size of the scatterers.

$$\frac{G_i(X, |f_{\infty s}|)}{G_j(X, |f_{\infty s}|)} = \frac{S_j \bar{v}_i}{S_i \bar{v}_j} \tag{4.4}$$

where $i \neq j$ and $i, j = 1, 2$ or 3, representing the three frequencies [Sheng and Hay, 1991]. The size-dependent functions $G_{i,j}$ on the left-hand side are pre-calculated using Equation 3.21. S_i and S_j are system sensitivity constants and $\bar{v}_i$ and $\bar{v}_j$ are mean signal levels. This method was found to be sensitive to noise, particularly for low signal level in $\bar{v}_j$. The new scheme presented here is not limited in this way. The range of concentrations over which reliable profiles can be determined is increased as a result. Estimates from small signal levels are restricted by signal-to-noise statistics and numerical error.

The division of size estimates into two distinct ranges ($D < 280\ \mu$m and $D > 280\ \mu$m) is interesting in that Sheng [1990] found a similar division in his inversion scheme, but at $D = 200\mu$m. The effect of this on both inversion approaches is that from three frequencies, only two independent quantities (a and M) can be determined. A third useful quantity would be σ_g, the standard deviation in the grain size distribution. In this analysis, and in those results from Sheng and Hay [1991] presented here, σ_g has been

assumed to be 1.2 (in $|f_{\infty s}|$, Equation 3.21) as given by Flammer [1962].

Sheng's inversion algorithm uses the same formulation for the scattering attenuation correction term, and does not include the geometric correction factor F either. His treatment of averaging is different, however. Sheng pre-averaged the voltage, rather than the voltage squared, before inversion.

A major difference between the inversion algorithms is in computing time. Where Sheng's inversion of a regular field data file (2600 sets) takes approximately 1 minute on a RISC based MIPS/120-5 workstation, this new procedure takes over an hour. Most of the time is spent in finding the zeros of ϵ_{mn}, which is currently done by bisection search [Press *et al.*, 1987, p. 246–247], and in reading the data file. Computation time could be improved significantly if the entire data file were to be read into one large array, and if more efficient zero-finding were used. This consideration has direct impact on future implementation of inversion in real time.

Chapter 5

Laboratory Results

Details of the experimental setup and procedures used in the laboratory trials have been discussed in Sections 2 and 2.1. Laboratory experiments have served to calibrate the acoustic system, determine the backscatter form factor for natural sand, and to test various aspects of the inversion algorithm.

An assessment of the reliability of the inversion algorithm can be made by comparing the calculated size and centreline concentration to the measured values. Measured and inverted values are plotted against one another in Figures 5.1a and b, with inversion estimates on the vertical axis in both cases. Calculated values were determined from 200-set runs, corresponding to a time interval of approximately half a minute per run. Calculated con-

centrations are the average of 196 centreline concentrations inverted from voltage data to which a 5–set running average has been applied. Calculated diameters are the average across the jet of the non-zero estimates, weighted by the number of independent values for each range bin in the averaged profile (inverted from the same averaged voltage data). Estimates were considered to be independent if they were as far apart in time as the 5-set averaging window is wide (that is, 0.75 s or more apart). Data from 4 groups of experiments have been used; one with sieved sand of a range of sizes (see Table 2.2) and three using natural sand samples from three locations as listed in Table 2.3. Background level for each group of experiments was determined from a 200 set run recorded with the pump system running, but carrying no sand.

The scattering attenuation correction (Equation 3.33) has not been included in calculating the results shown in Figure 5.1. The effect of attenuation is evident in Figure 5.1a for concentrations above 5 g/l (Figure 5.1c shows the region from 0 to 5 g/l). The diameter calculation, Figure 5.1b, shows over-estimation of the small sizes, and under-estimation of the larger. Slope, intercept and R^2 for the regression fit (dashed line) are listed in the Figure. The vertical spread in calculated values at 139, 157 and 360 μm indicates a concentration dependence in the size estimates – those from low

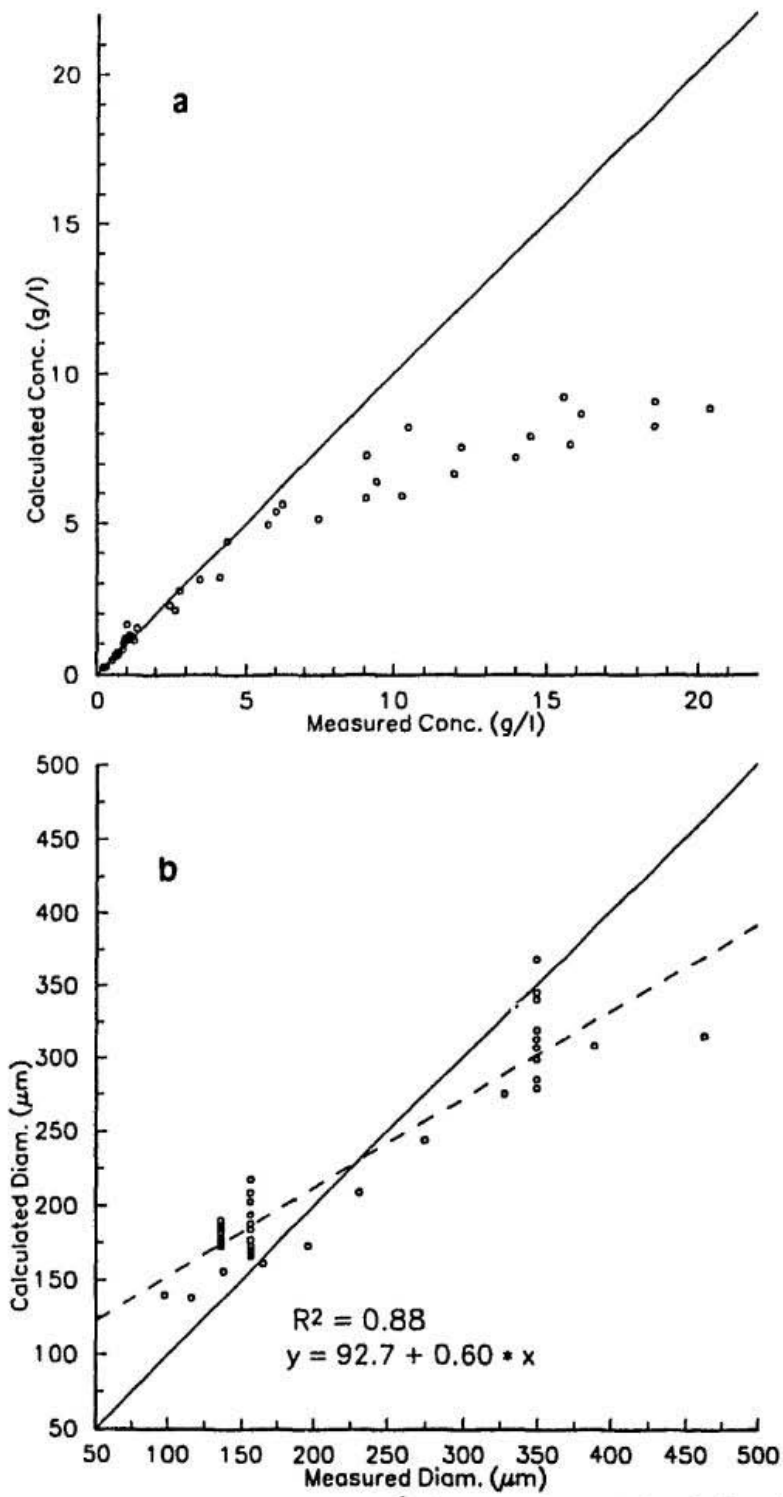

Figure 5.1: Comparison of measured laboratory data with calculated values. a) Centre-line concentration [g/l] b) Diameter [μm]. The solid lines are one-to-one lines in all cases.

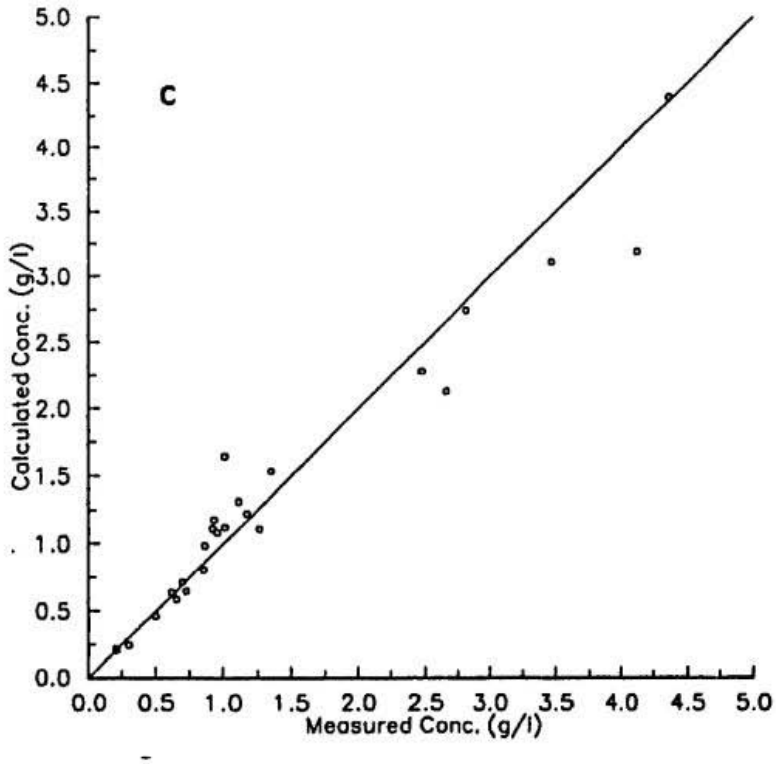

Figure 5.1: Comparison of measured laboratory data with calculated values.
c) Centreline concentration replotted from 0 to 5 g/l.

concentration runs are smallest and estimates increase for higher concentrations. This is most marked in the case of the largest size.

The comparison of inverted and measured concentrations indicates that the scattering attenuation correction plays a significant role in obtaining meaningful estimates above 5 g/l.

5.1 Geometric Considerations in the Tank Experiments

The specific geometry imposed in the jet experiments introduces some considerations which do not apply to the field experiments. These stem from the conical shape of the jet (rather than cylindrical) and the alignment of the three transducer units (see Figure 2.2) relative to the axis of the jet. The effect of geometry is particularly evident in size profiles.

Typical inverted profiles of size excluding scattering attenuation are shown in Figure 5.2. Calculated particle diameters plotted as a function of range are the average of nonzero results from 196 inverted estimates after 5-set averaging of the voltage data, only including those values representing the average of more than 10 independent estimates. The edge of the jet closest to the transducers is to the left. The profiles show interesting range

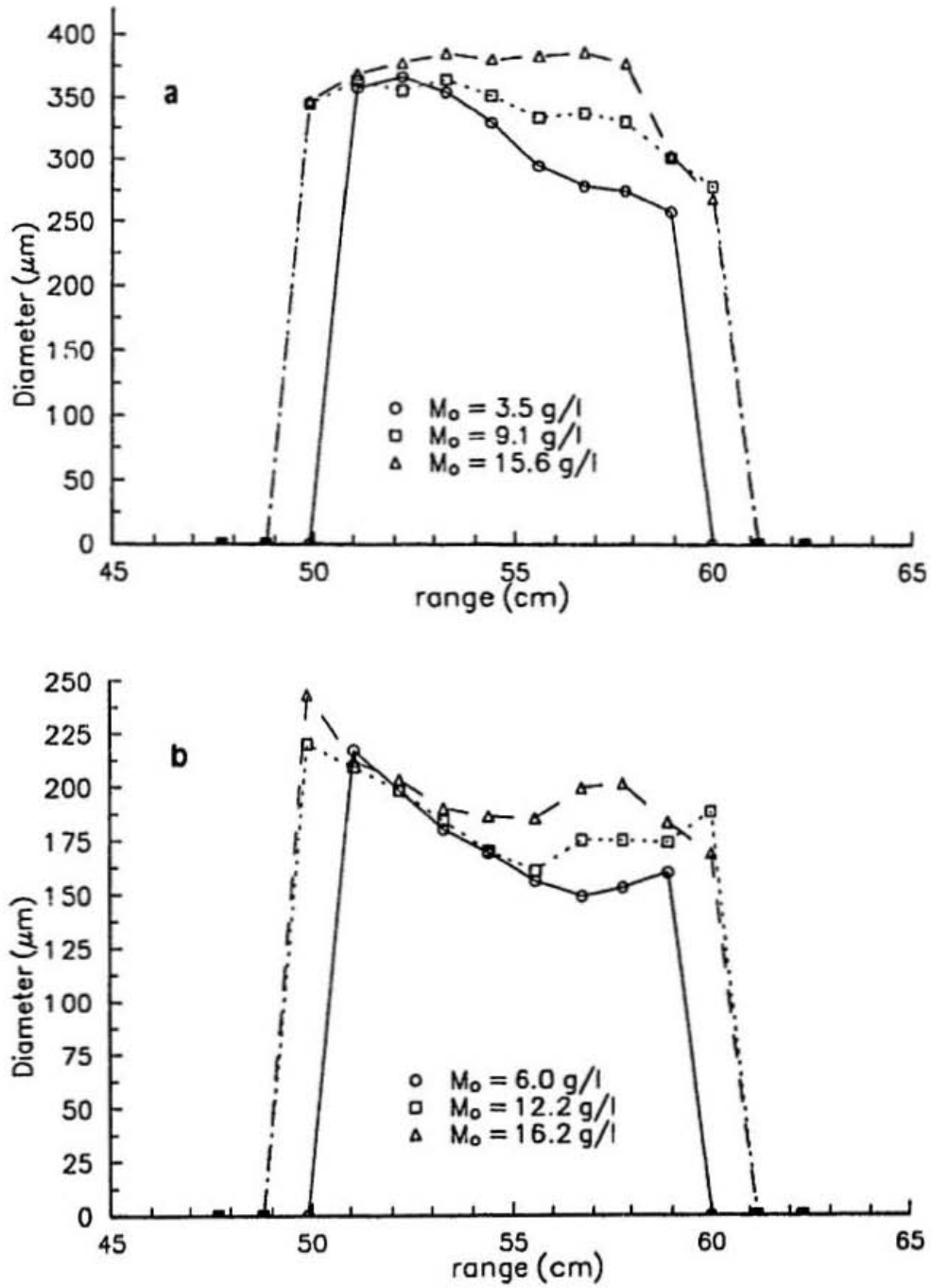

Figure 5.2: Inverted size profiles of the jet for sieved size a) D = 360 μm (QLB sand), b) D = 157 μm (PEI sand).

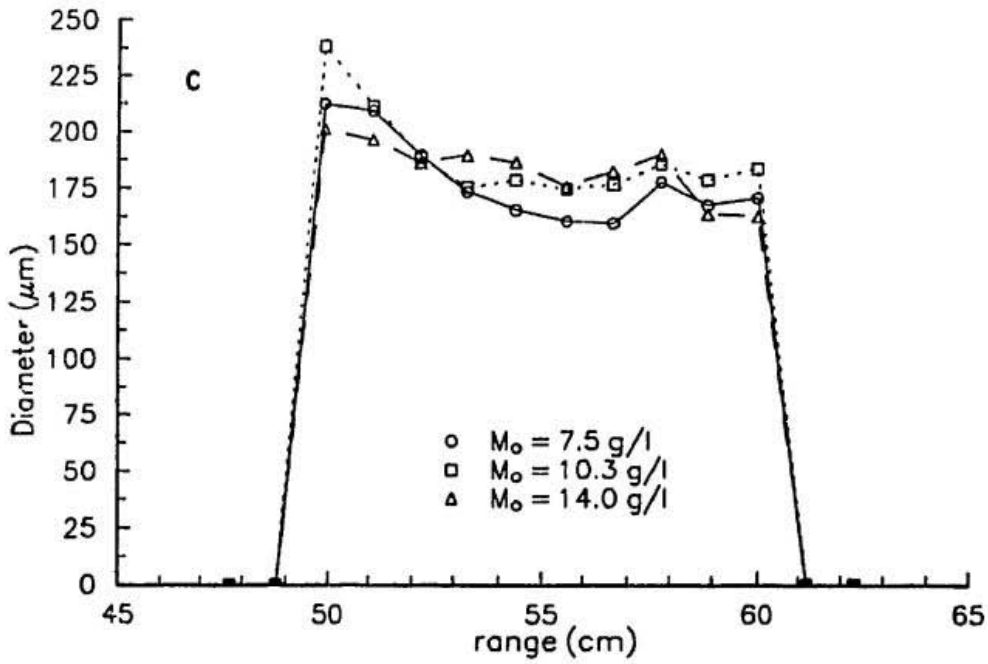

Figure 5.2: Inverted size profiles of the jet for sieved size c) $\mathfrak{D} = 139$ μm (BWB sand).

dependence. The size estimates at the leading edge of the jet are higher, but decrease across the jet for the lower concentration cases. This effect is most pronounced for the largest and intermediate sizes. This range dependence is due in part to geometric factors which would be corrected by the F term and also to the difference in the volume detected by the 1 and 5 MHz units. At the far edge of the jet, the transducer beams are wider, so that the change in concentration across the detected volume can be larger. Furthermore, the alignment of the transducers, as shown in Figure 2.2, is such that the beam of the highest frequency (5 MHz) unit crosses a slightly narrower and denser part of the jet on the near side, affecting a higher concentration gradient. At the same time, the 1 MHz unit beam crosses a wider, more diffuse, part of the plume. The inversion algorithm is particularly sensitive to ϵ_{a1}, so that differences between the volume insonified by these two units is more likely to be noticable in the inversion results.

As noted earlier, aspects of this geometric problem are specific to the jet experiments. In the field, differences in the detected volume of the transducer units contribute to error, and in regions of high concentration gradient, inhomogeneities in N within the detected volume must have an impact of inverted results.

5.2 Examination of Scattering Attenuation

The scattering attenuation correction described in Section 3.2 has been applied to the data shown in Figures 5.1a and b and results are shown, with regression statistics, in Figures 5.3a and b. This correction improves the concentration estimates up to 10 g/l, though appears to over-compensate for the attenuation effect. Failure of the inversion algorithm occurs for concentrations above 10 g/l; over-correction of the signal levels by this scattering attenuation term results in hugely exaggerated concentration estimates. This will be discussed in detail presently. The diameter estimation, shown in Figure 5.3b, is similar to the uncorrected results. The regression line falls lower across the 1:1 line (the slope is almost the same), but this is due to the loss of the high concentration values for which inversion failed — for example, compare the estimates for 360 μm in Figures 5.1b and 5.3b.

Experiments were carried out in the laboratory which were designed to permit a direct test of the scattering attenuation correction. As described in Section 2.1, a small transducer (pinducer) was placed opposite the 2.25 MHz unit at range r_H, with the centreline of the jet between them [see Hay, 1991]. The ratio of the voltage output, v_H, from the pinducer with the pump system off and on, carrying sand, represents the one-way attenuation due

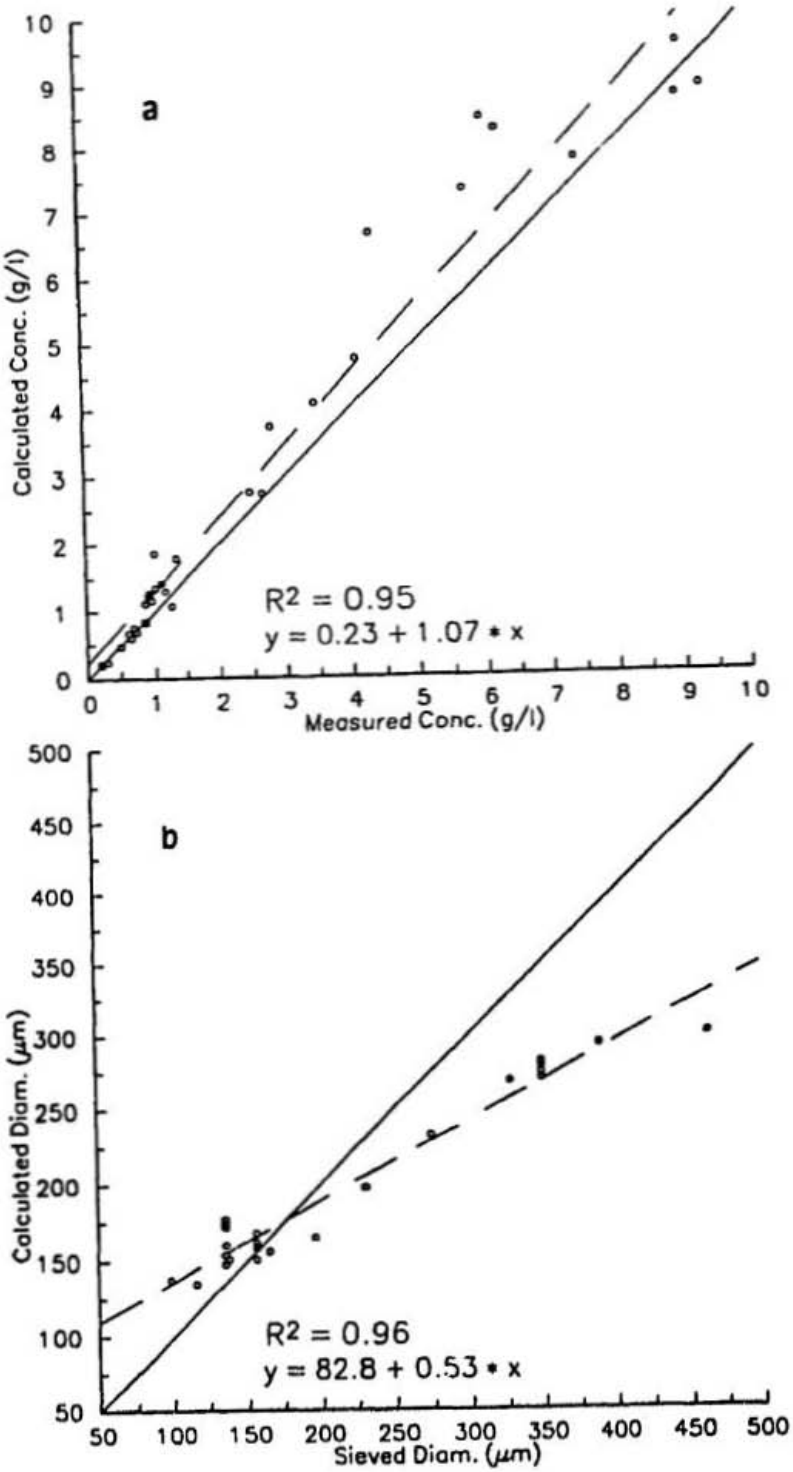

Figure 5.3: Comparison of measured laboratory data with calculated values including scattering attenuation correction. a) Centre-line concentration (g/l) b) Diameter (μm).

to particles across the full width of the jet [Hay, 1991] —

$$\frac{A}{2} = \ln\left[\frac{v_H(0)}{v_H(M_o)}\right] \tag{5.1}$$

where M_o is the measured centreline concentration. Calculated values are half the accumulated attenuation at a bin corresponding to approximately r_H. Results are shown in Figure 5.4 as two pairs of regression lines fitted to measured and calculated values. For each of two sizes, using 360 μm QLB and 139 μm BWB sand, measured and calculated $A/2$ are plotted as a function of measured centreline concentration. The calculated values are twice as large as the measured values and this discrepancy is the cause of the previously mentioned inversion failure when dealing with higher concentration profiles.

It was thought that failure of the inversion algorithm was a result of geometric effects related to the difference in alignment between the transducer beams. These would act principally in the farther side of the jet where the beams are wider. To determine whether this was the case, $A/2$ was accumulated to the centreline and doubled (assuming that the jet is symmetrical) for comparison with the measured values. These are plotted in Figure 5.5. At the centreline, scattering attenuation accumulated with range has not always reached such large values that inversion failure has occurred so cal-

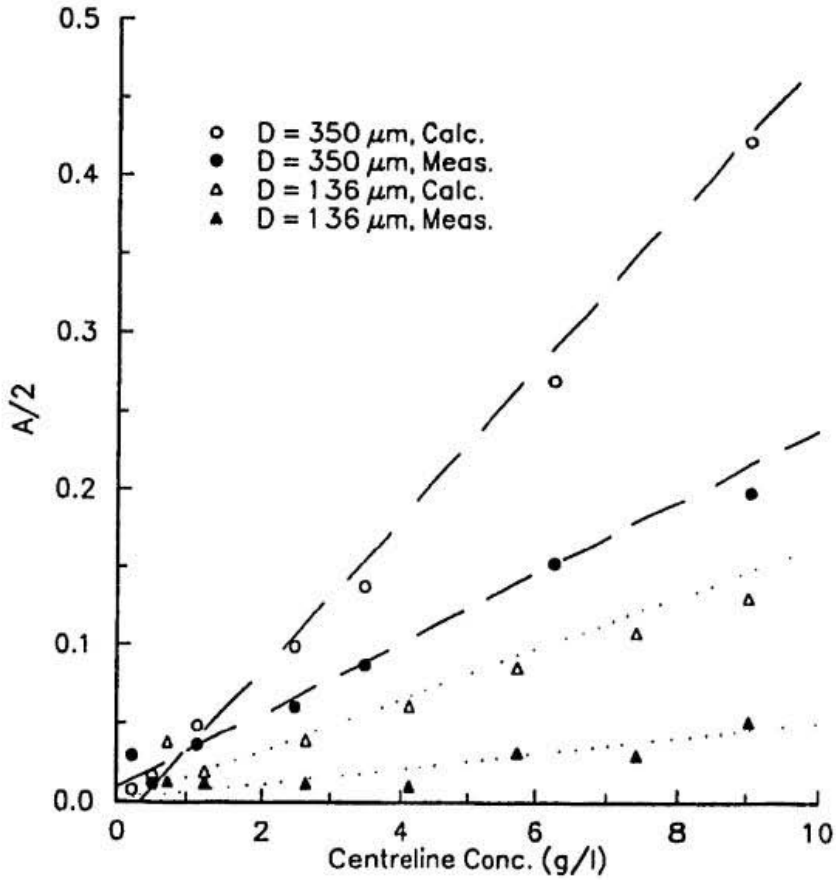

Figure 5.4: Measured and calculated scattering attenuation, accumulated across the full width of the jet. Measured values are shown by filled symbols, and calculated values are open symbols.

culated values are available for almost the full range of concentrations (the points shown for the highest concentrations are the average of fewer values, however). The results shown in Figure 5.5 confirm those in Figure 5.4, and indicate that geometric factors particular to the jet scattering geometry do *not* affect the scattering attenuation calculation.

Note that the linearity of the measured attenuation with concentration indicates that multiple scattering is not significant up to 18 g/l.

The failure of the inversion algorithm can be summarized by the following. When high concentration levels (> 10 g/l) are encountered, over-correction for scattering attenuation occurs — in cases of high mean concentration the effect accumulates across the jet until failure occurs when corrected signal levels blow up, particularly in the 5 MHz channel. High concentration fluctuations occurring in lower mean concentration runs likely cause distortion in the regions of the jet shadowed by them. The problem appears to be a result of the way that the scattering attenuation is applied, rather than with the high-pass model for α_s, since total scattering cross-sections computed from the measured attenuation in the jet agree well with the model [Hay, 1991]. Similar over-correction was obtained using a different theoretical model for α_s which had been used by Sheng [1990] in earlier work. Note that in the numerical implementation of the scattering atten-

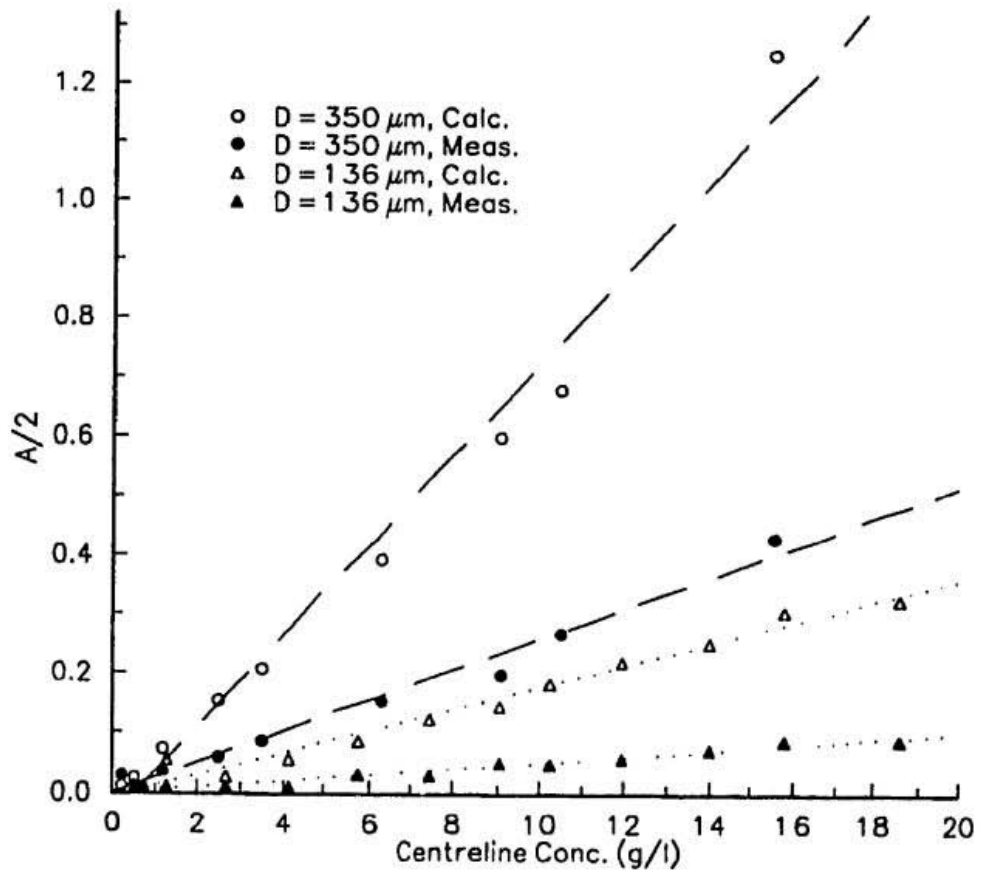

Figure 5.5: Measured and calculated scattering attenuation. Calculated values are accumulated to the centreline and doubled.

uation integration, the summation is lagging by half a range bin from the centre of each bin – including this additional contribution to the attenuation *increases* the over–correction.

Similar over–correction of the squared mean backscatter intensity at 5 MHz (neglecting F) has been noted by Hay [1991]. Thorne *et al.* [1991] have used the same high-pass model for α_s and found good results for particle diameters of 210, 125 and 55 μm at 3 MHz, though the concentrations used were between 0.01 to 1 g/l — small enough that scattering attenuation effects are negligible. They make the relevant observation, however, that at higher concentrations, the scattering attenuation becomes more important and uncertainty in this term can lead to significant error.

Concentration profiles for two of the cases using QLB sand shown in Figure 5.2 (M_o = 3.5 g/l and 9.1 g/l) are shown in Figure 5.6. The lowest (solid) curve in each case has not been corrected for scattering attenuation, while the highest (dashed) curve has been. The dot–dashed line in the Figure is a Gaussian profile calculated from $M(r) = M_o \exp(-(r-r_o)^2/2\sigma_M^2)$, where M_o is the measured centreline concentration and r_o is the measured range to the jet centre, 55.0 cm. Hay [1991] found that suction sampled concentration values across the jet followed a Gaussian profile with σ_M = 1.9 cm. The effect of scattering attenuation is small in the low concentration case, and the

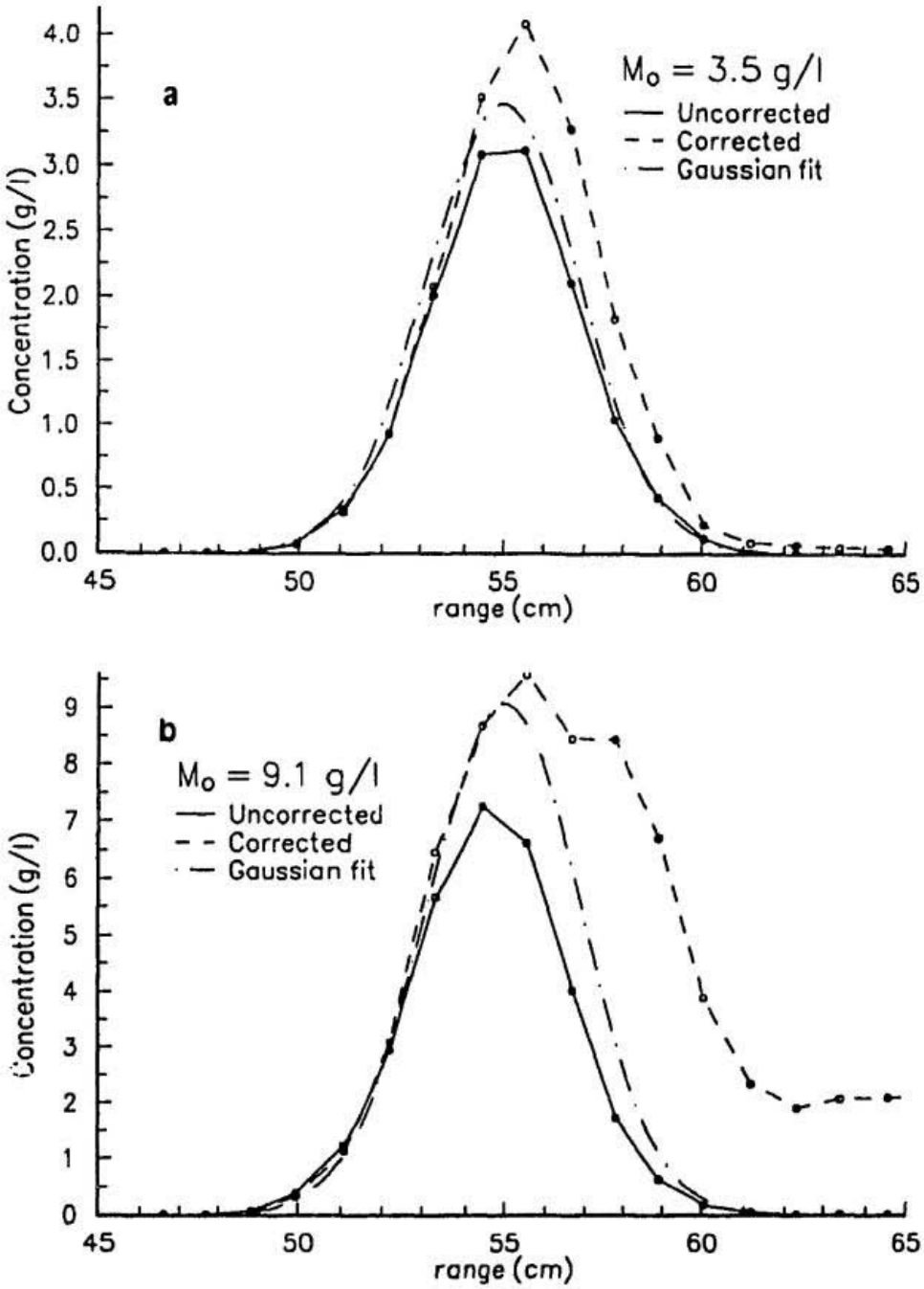

Figure 5.6: Concentration profiles across the jet from experiments using QLB sand. Shown are the inverted results with (dashed line) and without (solid line) scattering attenuation correction, and a Gaussian profile.

over-correction of the scattering attenuation term is evident in the corrected profile. The centreline of the corrected curve has been shifted away from the transducers and concentrations on the farther side of the jet are elevated. This effect is further evident in the higher concentration example where the concentration level on the far side of the jet is obviously incorrect. The apparent centre of the jet in the uncorrected profile has been shifted toward the transducers. For centreline concentrations above 10 g/l, the averaged inverted concentrations greatly exceed those measured at the jet centreline (10 times too large is not uncommon).

Having discussed the failure of the algorithm at length, it should be pointed out that the inverted results for concentrations less than 10 g/l (Figure 5.3) are reasonably good. Mean concentration levels in field data are rarely above 10 g/l outside the bottom boundary layer, though fluctuations undoubtedly exceed this level. Nevertheless, this type of failure was not seen when inverting the field data, as discussed in the next Chapter.

5.3 Examination of the Form Factor

Results similar to Figure 5.1 have been computed using the rational fraction fit to the form factor, $|f_{\infty r}|$ (Equation 3.22), and are shown in Fig-

ures 5.7a and b. Below 6 g/l, inverted concentration values using $|f_{\infty r}|$ fall above the 1:1 line, and in general, are larger than those values estimated using the semi–empirical form factor. Given the effects of scattering attenuation, the values above the 1:1 line are less believable than those below. The diameter prediction using $|f_{\infty r}|$, however, is better than the previous results, shown in Figure 5.1b. The regression fit to the estimated sizes using $|f_{\infty r}|$ has slope closer to the 1:1 line.

Percentage differences between $|f_{\infty s}|$ and $|f_{\infty r}|$ are shown in Figure 3.4 — note that the reciprocal of the form factor squared is used in calculation. The process of finding zero crossings of functions which are the difference of signal levels from pairs of channels removes any direct effect of the difference between form factors. The large difference in the region $X < 0.3$ is noteworthy, but only applies to the smallest sizes at 1 MHz. On the basis of the improvement in the diameter calculation, the rational fraction form factor provides better inverted results. However, results presented in the remainder of this section have been calculated using the semi–empirical form factor.

This investigation has raised the question of the real behavior of $|f_{\infty}|$ in the region $X > 2$. The experimental data are sparse in this area and possibly more widely scattered. Future experiments are planned to clarify

this issue.

5.4 Comparison with Results of a Previous Inversion Method

Sheng and Hay [1991] have presented laboratory results similar to those presented here, but using a different inversion algorithm. Their results are shown in Figure 5.8. All 200 sets of backscatter voltage data were averaged before inversion — it is not clear whether this smoothing of high concentration fluctuations stabilizes the scattering attenuation correction in this older inversion scheme. Similar averaging before inverting with the new algorithm did not increase the operating range past 10 g/l.

Comparing Figures 5.3 and 5.8, the concentration calculation is similarly slightly over-estimated by both methods. Sheng's results have less scatter and cover the full range of experimental concentrations. Larger scatter in the results presented here are likely due to the lesser degree of averaging of the voltage data before inversion. Averaging over longer periods also would tend to reduce the mean concentration values due to the spiky nature of the concentration fluctuations. Sheng's approach, in using $< v >$ rather than $< v^2 >$, is not as sensitive to over-correction by the scattering atten-

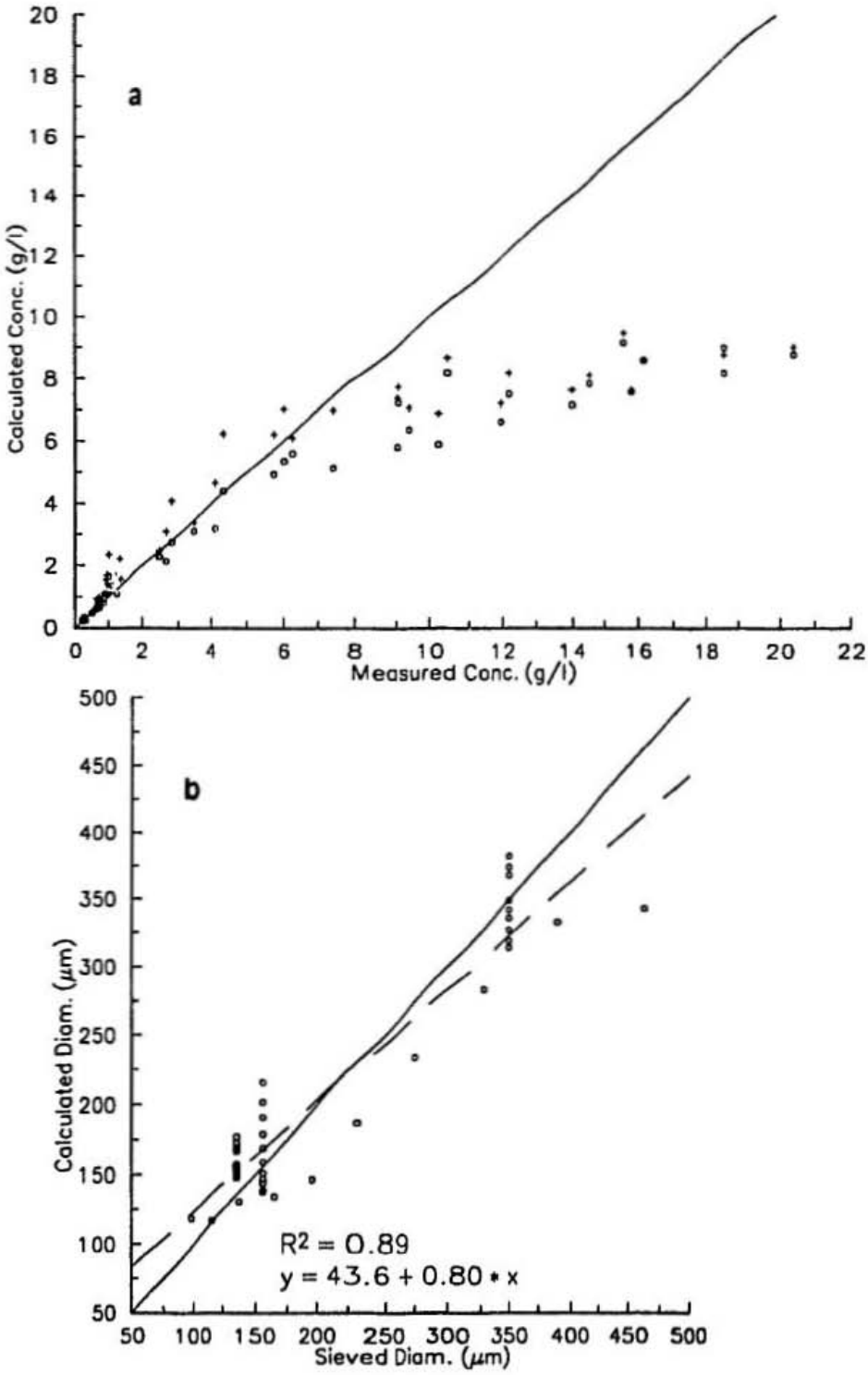

Figure 5.7: Comparison of measured laboratory data with inverted values, using $|f_{oor}|$. a) Centreline concentration [g/l]. + denote values calculated with $|f_{oor}|$ and, for comparison, o denote values calculated with $|f_{ooa}|$ (as in Figure 5.1a). b) Diameter [μm] calculated using $|f_{oor}|$.

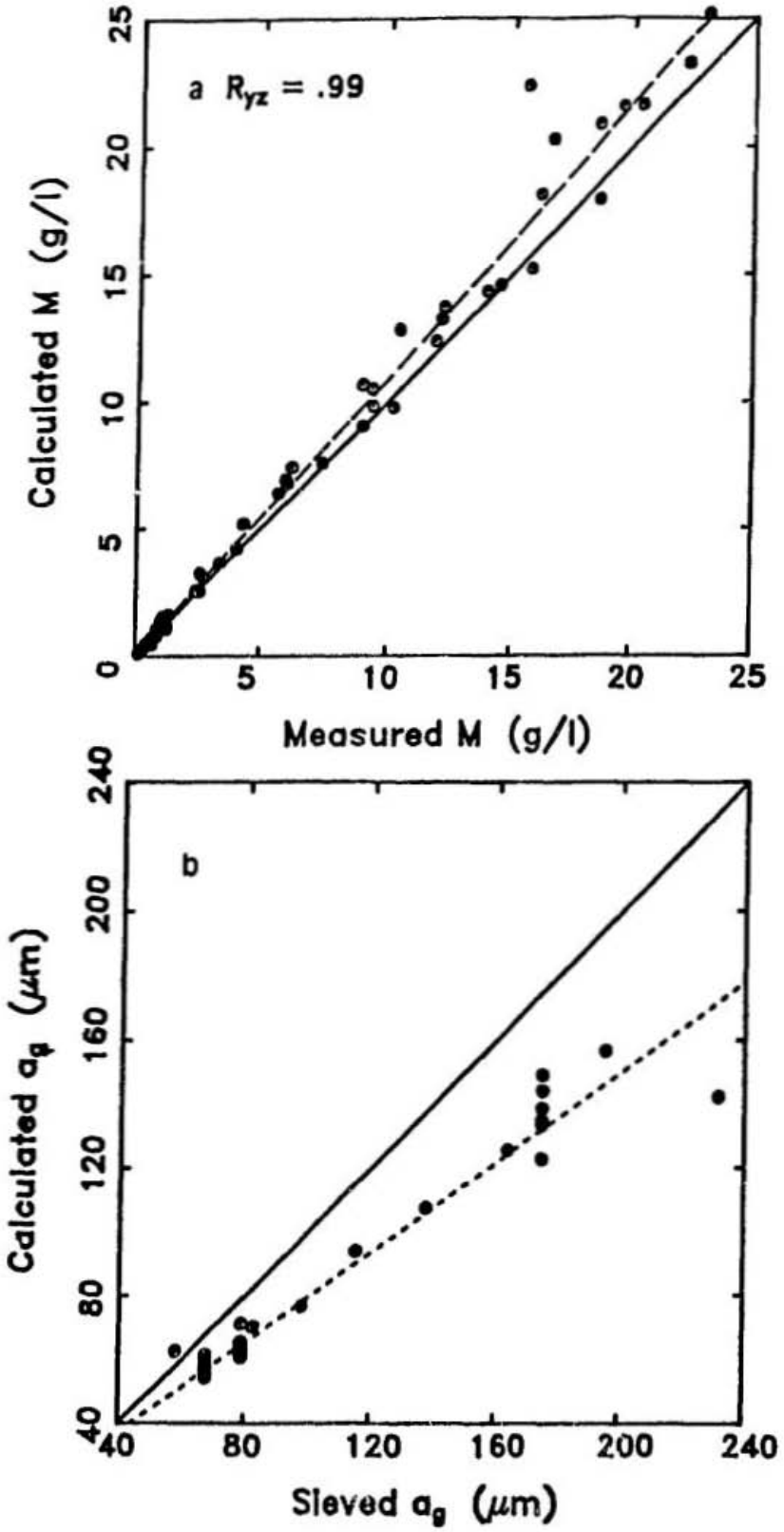

Figure 5.8: Comparison of inverted and measured jet centreline concentration and radius, using Sheng's inversion procedure [from Sheng and Hay, 1991]. Radius estimates are for runs with concentrations over 0.8 g/l.

uation exponent, which is half the size. In addition, by calculating ratios of voltages, errors in the attenuation correction factors in the numerator and denominator may to some degree cancel, allowing inversion of the full range of concentrations.

The radius inversion results in Sheng and Hay [1991] show similar under-estimation for larger sizes and over-estimation of very small sizes. The similarity of these results, obtained independently through different methods, indicate that further examination of the backscatter form factor, which contains most of the size dependence of the backscatter signal, is in order. In the case of the very largest sand sizes, a small amount of the under-estimation may be real, due to settling of the largest particles in the hose system. The tendency of size estimated by the new algorithm to increase with concentration is interesting in that the opposite tendency is shown by the previous algorithm.

To summarize this comparison, the present concentration estimates have larger scatter but follow the same trend of slight over-estimation as the results from Sheng and Hay [1991]. The new algorithm operates over a lesser range of concentrations, limited to < 10 g/l. The size estimates over the range of diameters used in the experiments also exhibit a similar trend to the previous results, but estimates of a particular sand size increase with

concentration, rather than to decrease, as was the case with the ratio algorithm.

5.5 Averaging and Examination of the Stability of the Jet

Averaging is necessary to remove purely statistical variations due to the random relative motion of the scatterers. Hay [1991] has demonstrated, by correlating signal levels at two vertically separated points off the jet axis, that large fluctuations seen in the backscattered intensity represent real structures in the concentration field. Similar fluctuations are seen in field data, where these can contribute significantly to sediment flux. Averaging over long time periods reduces the estimated flux by smoothing these fluctuations.

Profiles resulting from inversion of the laboratory backscatter data represent a single line across the jet and are acquired at 6.6 Hz. This sampling is not sufficient to separate or positively identify individual turbulent features of finite size in the jet. This undetermined amount of naturally occurring fluctuation increases the variability of the concentration level. The question of how much averaging is enough can be addressed by examining the

variability seen in the inverted size profiles.

Figure 5.9 shows standard deviation as a function of the square root of the sample size where $(n)^{\frac{1}{2}}$ = [no. of sets averaged over]$^{\frac{1}{2}}$ at a range of 53.0 cm (2 range bins toward the transducer from the jet center) for 3 different experimental runs, without the scattering attenuation correction. For these runs, at 53.0 cm, the diameter estimation was robust — there were no zero entries in these inverted profiles at this range. (In the case where signal levels are low enough that inversion is not attempted, zero diameter values are returned by the algorithm.) Zero diameter entries are *not* included in the averaged size profiles. Zero concentration values, on the other hand, are significant and all entries below saturation level are counted. The number of independent estimates is therefore potentially lower for the averaged diameter estimates, but not in the case of the runs used here.

The standard deviation in diameter, as shown in the Figure, has been reduced to approximately 10% of the mean after averaging the voltage data over as few as 10 sets (1.5 seconds). The standard deviation in concentration is less than 20% of the mean at this level of averaging. The variability in size estimation is expected to be small for these experiments, which used sieved sand with very narrow size distribution. The concentration field in the jet contains large real turbulent fluctuations [Hay, 1991], so naturally the

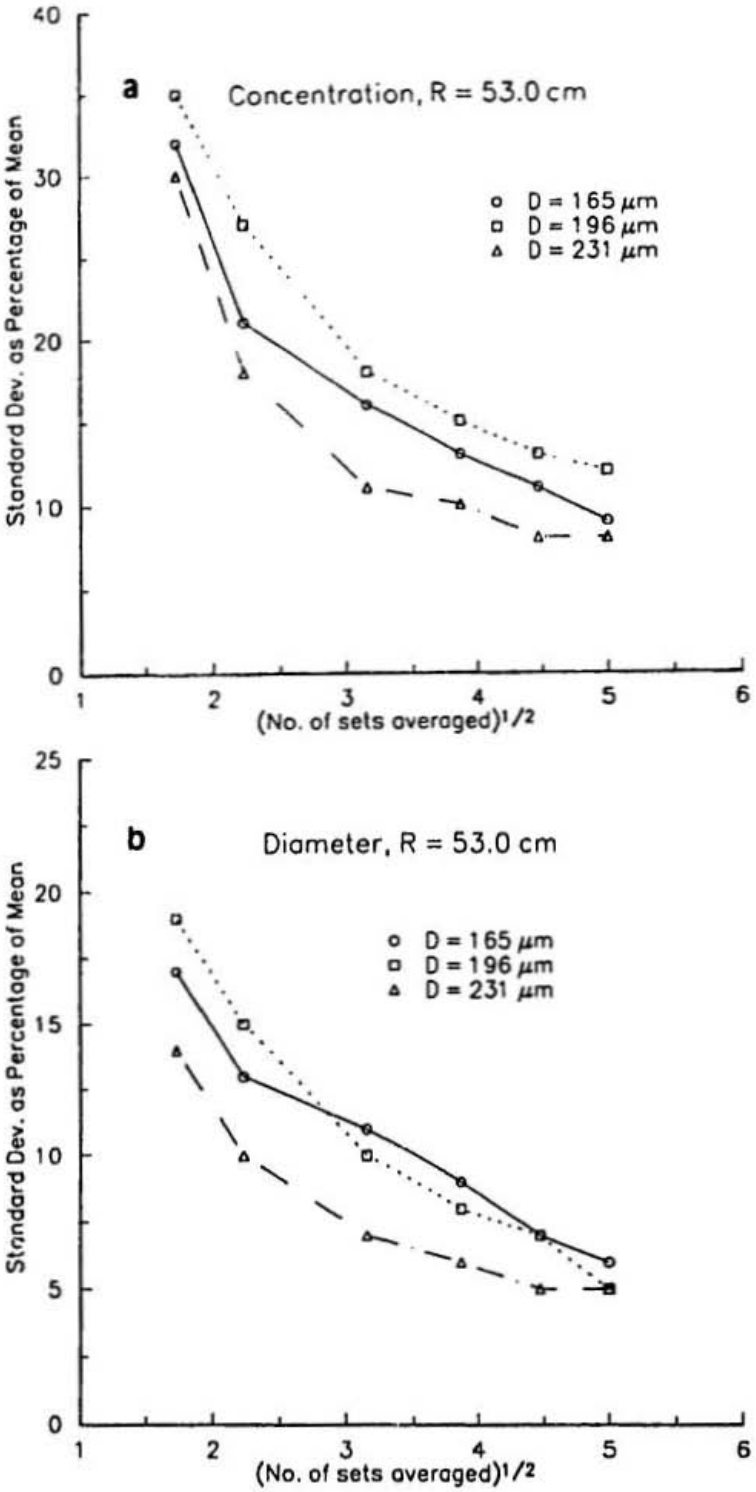

Figure 5.9: Sample standard deviation as a function of sample size. Concentration statistics (a) and diameter statistics (b) are plotted as a percentage of the mean.

concentration estimation has larger variability. The size and concentration estimates presented earlier in this Chapter were computed from voltage data to which a 5-set running average was applied. Figure 5.9 shows the standard deviation in this case to be about 25% in concentration estimates, which falls well within the natural variability of the concentration field of the jet, and 15% in diameter estimates.

A time series of concentration at 53.0 cm from 10-set (running) averaged voltage data is shown in Figure 5.10. Large fluctuations in the concentration level are seen to be predominantly positive relative to the mean, and to some degree, periodic. These characteristics would indicate some sort of flapping mode in the jet, or resonance in the recirculating system, as the source, rather than turbulent structures in the jet. A small drop in mean level is evident over the 30 second run. This is plausible as a small amount of material is lost from the system over the course of each run.

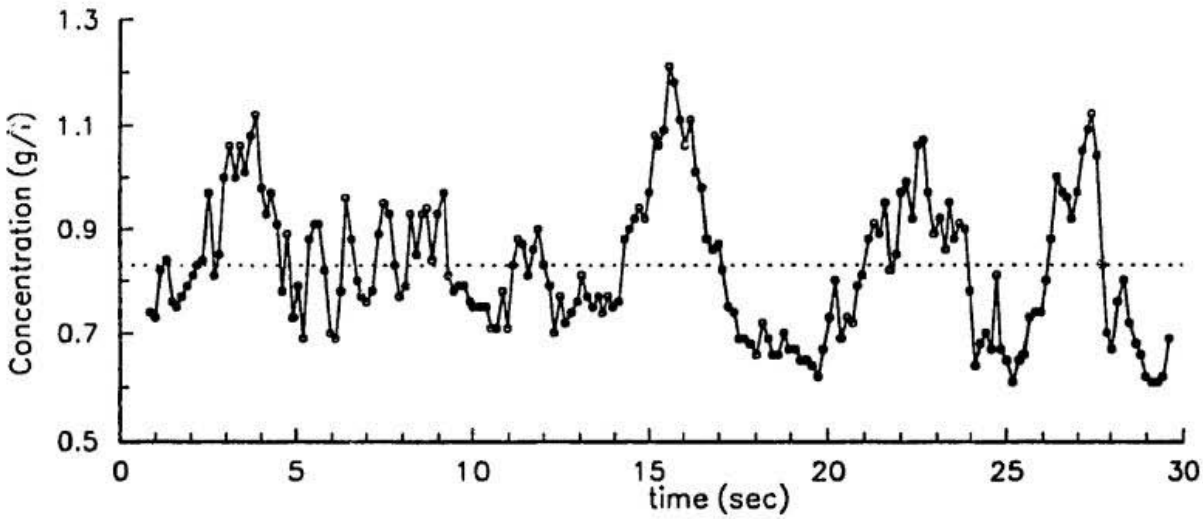

Figure 5.10: Time series of concentration at range 53 cm. Sieved sand size is 196 μm and mean concentration (dotted line) is 0.83 g/l.

Chapter 6

Field Results

The field deployment of RASTRAN at Stanhope Lane has been described in Section 2. Comparison of inverted field data will be made with results obtained using Sheng's inversion algorithm and with OBS data. The OBS comparison provides a measure of the accuracy of the concentration estimation at a point in the profile corresponding in height to the location of the optical sensor.

Run	h_{OBS} (cm)	r'_{OBS} (cm)
300.030	5.0	87.8
301.015	4.8	87.8
308.046,.047	9.5	87.6

Table 6.1: Distances for RASTRAN-OBS133 concentration comparison. h_{OBS} is distance from OBS133 to bottom and r'_{OBS} is to the center of the range bin compared with OBS133 data.

6.1 Comparison of Inverted Concentration with OBS133 Measurements

Voltage data from the field experiments was block averaged over a 1.1 second (7 set) interval to reduce fluctuations in the backscatter signal due to relative motion of the scatterers, and to lessen the effects of the horizontal separation of the transducers (see Figure 2.3). Entire runs and segments of runs representing varying levels of suspension activity were averaged to compare with OBS concentrations averaged over the same time intervals. The ranges (r_{OBS}) at which to compare the inverted results with the OBS133 data, as determined by Sheng and Hay [1991], are listed in Table 6.1. Run 300.040 has not been used in this comparison, due to uncertainty in the distance to bottom.

Comparisons between RASTRAN and OBS concentrations have been made to inverted results obtained using both the semi-empirical form fac-

tor $|f_{\infty s}|$ (Figure 6.1a) and the rational fraction fit form factor $|f_{\infty r}|$ (Figure 6.1b). Also shown are the results obtained by Sheng [Sheng and Hay, 1991] (Figure 6.1c). The largest difference is between the newer inversion results with either form factor and those from Sheng's algorithm. Where inverted concentrations had been lower than those determined from the OBS data, the present inversion procedure produces estimates larger than the OBS values. The scatter in the newer results is larger, actually containing the 1:1 line with $R^2 = .88$ where Sheng has $R^2 = .96$. This over-estimation is consistent with the laboratory results for concentrations less than 5 g/l (Figure 5.3). Similarly, the increase in inverted concentrations using the rational fraction fit form factor is confirmed by the laboratory findings shown in Figure 5.7. The results obtained using both inversion procedures are encouraging, particularly considering the 1.4 m horizontal separation between the RASTRAN system and OBS133 and the proximity to the bottom boundary layer.

6.2 Averaged Size and Concentration Profiles

Average profiles of size have been compiled for the runs listed in Table 2.4 and run 300.040 (an additional low energy case) and are shown in

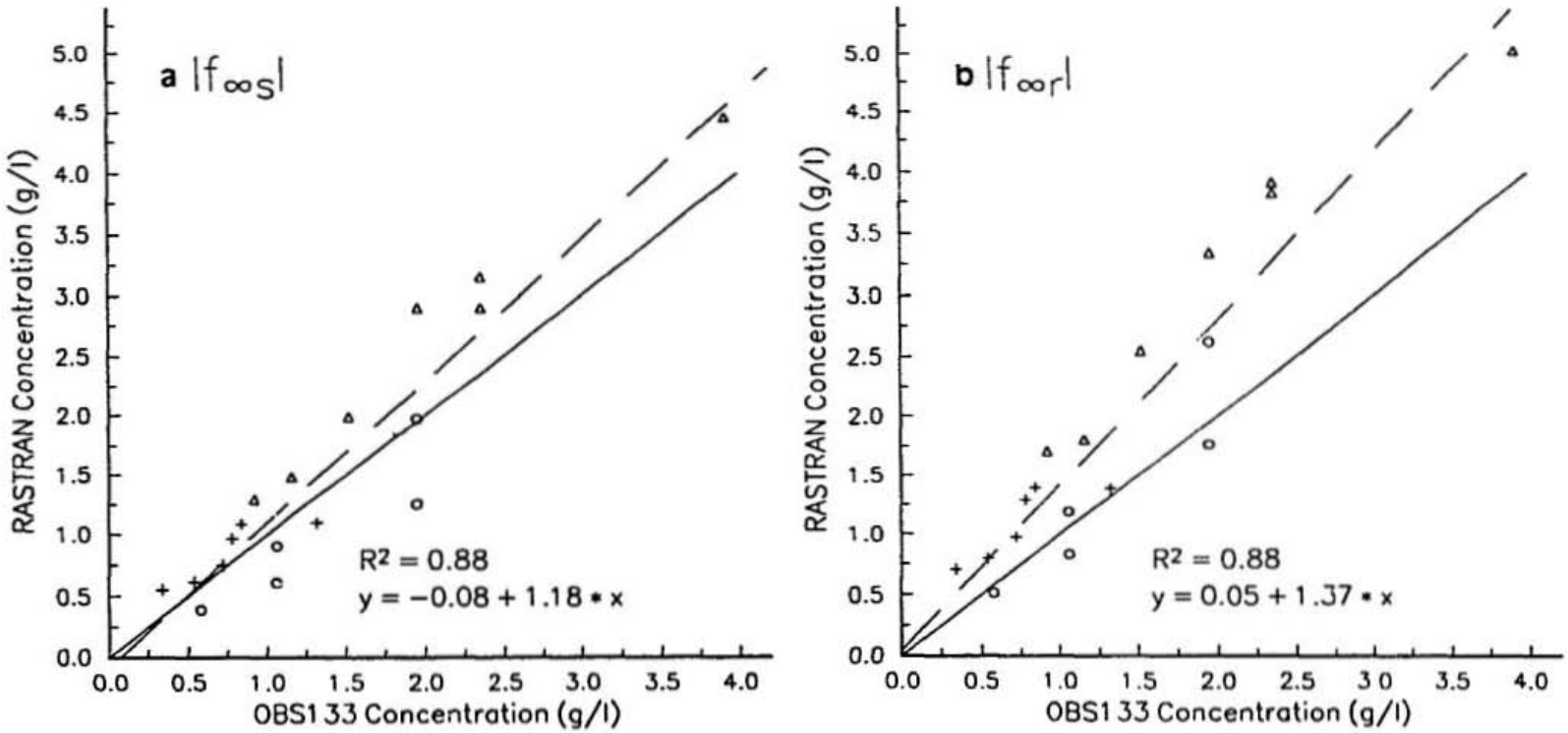

Figure 6.1: Comparison between inverted and OBS133 measured concentration. o are low energy runs, Δ are intermediate and + are high energy. a) using semi-empirical form factor, $|f_{\infty s}|$ and b) using rational fraction fit form factor, $|f_{\infty r}|$.

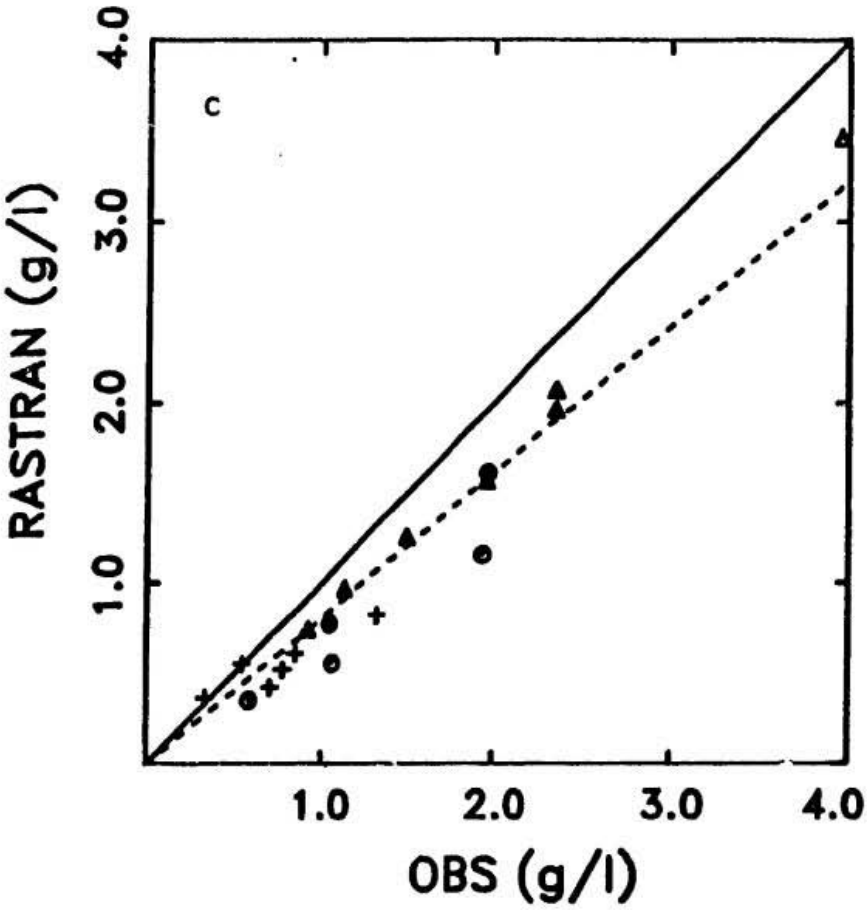

Figure 6.1: c) Comparson between inverted and OBS133 measured concentration obtained by Sheng and Hay [1991]. The same symbol convention as in Figures 6.1a and b has been used.

Figures 6.2, 6.3 and 6.4. Only those average values compiled from more than 10 independent estimates have been plotted in the size profiles, while those from more than 2 independent estimates appear in the standard error plots. The profiles represent the average over the 6.5 minute duration of each run. The standard error is computed by dividing the standard deviation from the mean by the square root of the number of independent estimates.

The mean size of suspended material is lower in the newer results than in the results obtained using Sheng's algorithm [Sheng and Hay, 1991], which show a mean size of 180 μm at a height of 5 cm. The new results show a mean size of 160 μm for the rational fraction fit form factor, and 170 μm for the semi-empirical form factor at this height. These newer results agree well with the 170 μm mean size of the sample taken from the bed at the deployment site. The 10 μm difference in the estimates using the two different form factors is consistent with the laboratory findings for estimation of sizes near 170 μm (compare Figures 5.7b and Figure 5.1b). Estimates of sizes below about 200 μm using the rational fraction form factor fell closer to the 1:1 line (lower) than results using the semi-empirical form factor. The profiles are not considered to be accurate below 5 cm height due to bottom echo contamination of the backscatter signal. Ripple bedforms approximately 2–3 cm in height and with wavelengths between about 5 and

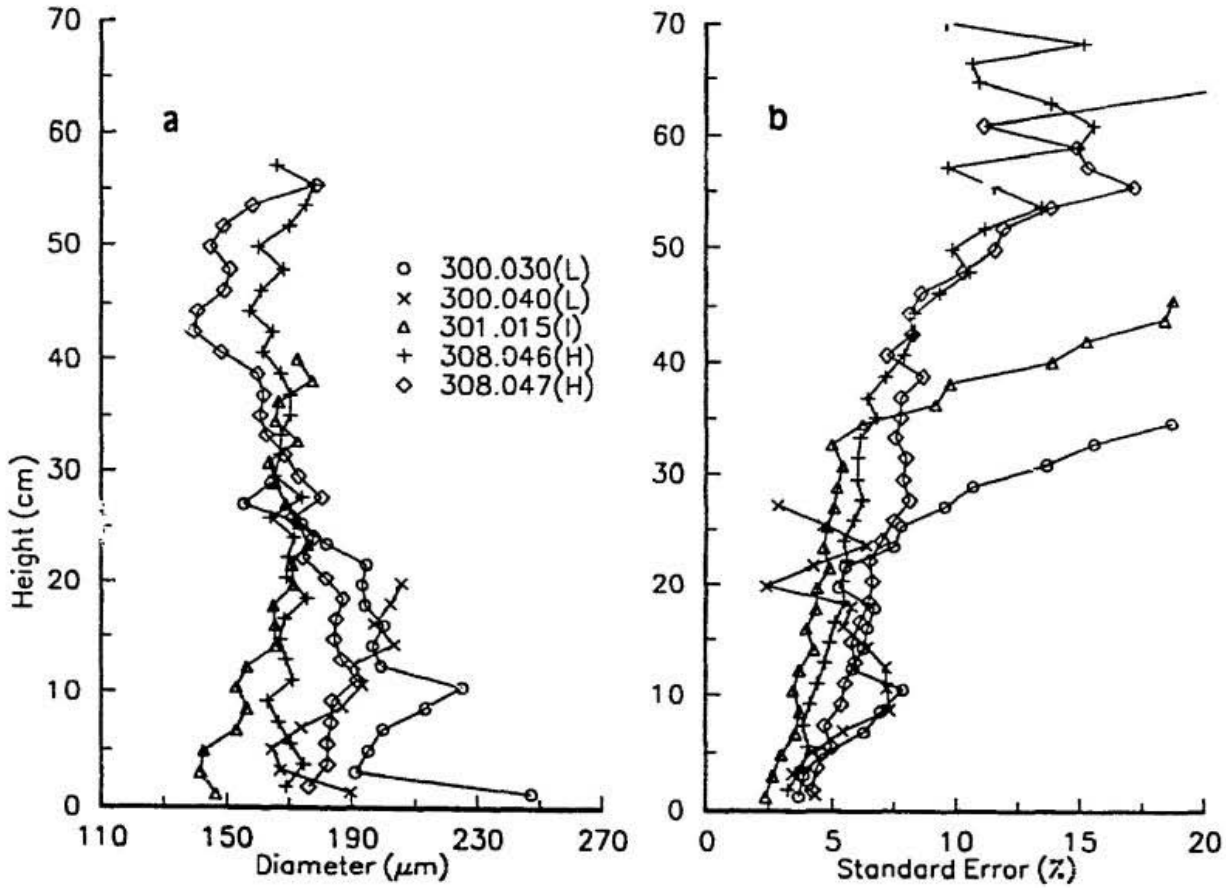

Figure 6.2: Size profiles (a) and standard error (b) for complete runs calculated using semi–empirical form factor.

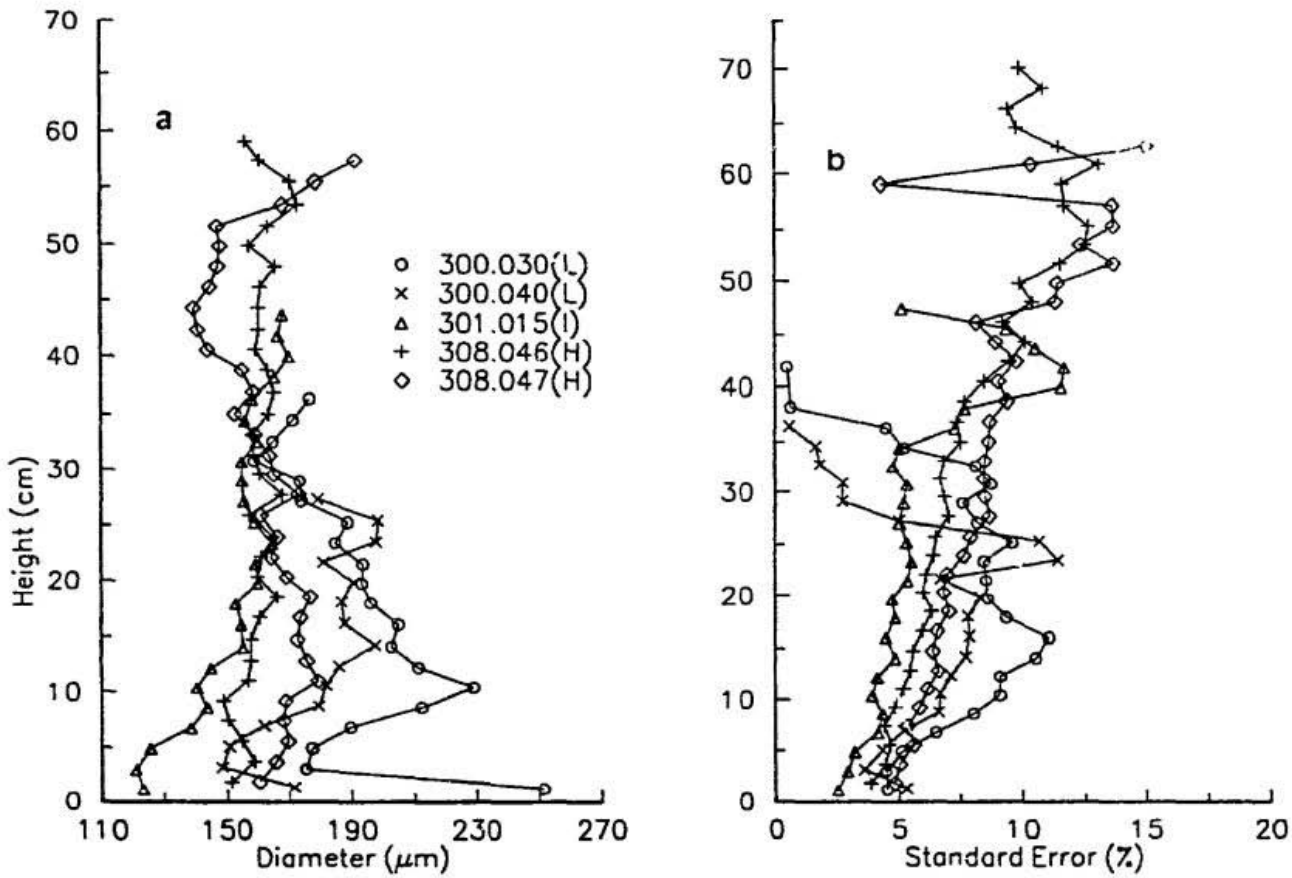

Figure 6.3: Size profiles (a) and standard error (b) for complete runs calculated using rational fraction fit form factor.

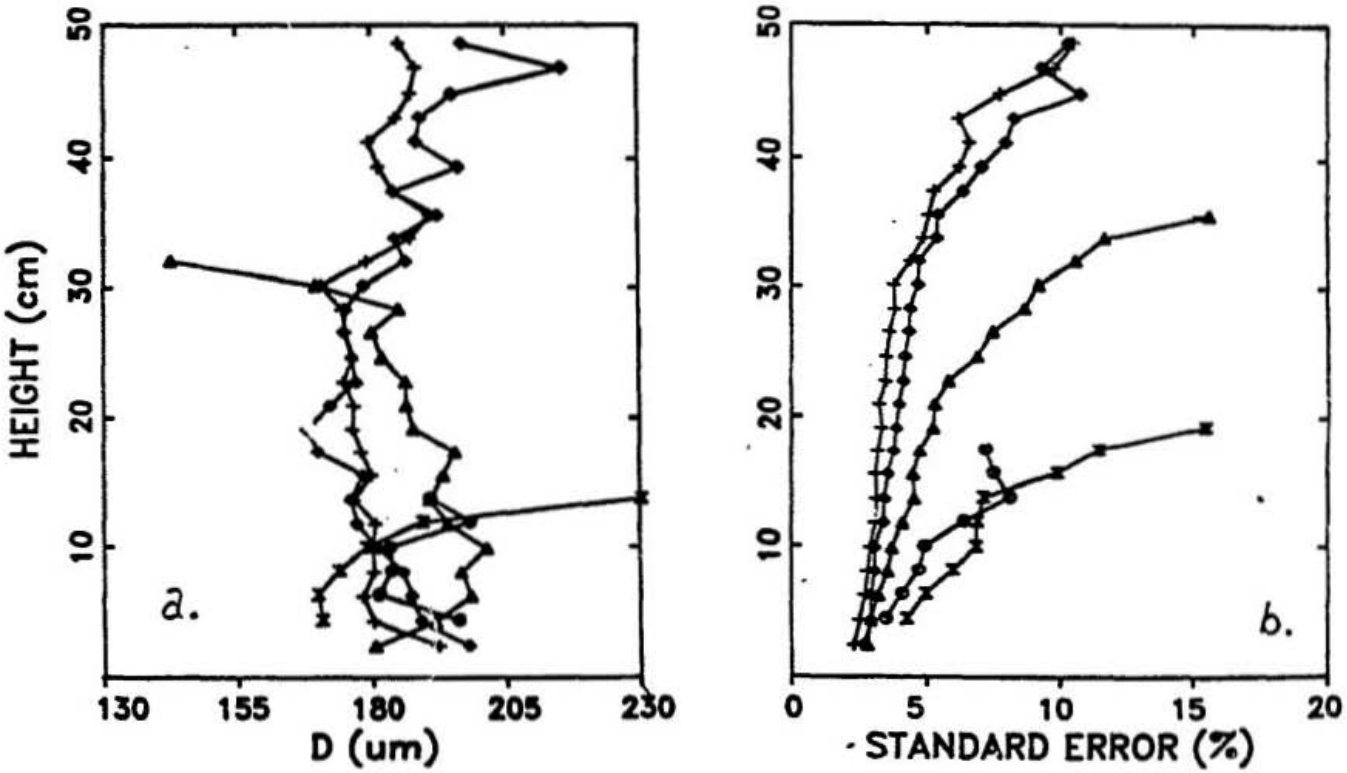

Figure 6.4: Size profiles (a) and standard error (b) for complete runs from Sheng and Hay [1991] for which the same symbol convention as in Figure 6.3 has been used.

15 cm were observed at the RASTRAN site during the field deployment [Hay and Bowen, 1991]. The widely fluctuating estimates farthest from the bed have large error. The vertical range of the new profiles above 5 cm from the bottom is greater. This extends the range of operation farther into regions of lower concentration, particularly in the low energy cases. Estimation of size and concentration in these areas has been a goal of this present effort which appears to have been achieved, though at the cost of increased standard error over most of the profile.

The size profiles for the high energy cases are approximately constant with height, where the earlier results show an increase in size far from the bottom. Laboratory observations of suspension of sand by waves support a weak decrease in size with height [Staub *et al.*, 1984]. Variation at the top of these profiles is associated with an increase in standard error, up to $\sim$ 15%.

The size profiles in the intermediate energy case show a large difference between these results and and those of Sheng and Hay. Their estimates of size through most of the profile are the largest of all energy cases (by up to 15 μm), while they are smaller using this inversion technique with either form factor. The increase in size with height seen in the newer profiles, however, is unlikely to be real, as prevously noted.

The standard error plots show larger variability in the estimates from the new algorithm, though the vertical range over which standard error is below 10% has been increased for the intermediate and, particularly, the low energy cases. The standard error for the results using the rational fraction fit form factor shows some obviously anomolous results (less than 3% at the top of the profile). The increase in standard error with height is largely a function of the reduction in the number of independent estimates, as occurrence of sediment at these heights is sporadic. Sheng and Hay [1991] found that a standard error of < 5–7% is necessary for consistency in their size profiles. This criterion eliminates from their results both the decrease in size with height in the intermediate energy case and the increase to 230 μm in the low energy case. This same restriction can not be applied to these present results, as standard error is greater on the whole. As pointed out by Sheng and Hay, averaging over longer time periods is necessary to reduce the variance in the size profiles. Examples of longer averaged profiles will be presented later.

Concentration profiles averaged over the 6.5 minute duration of each run are shown in Figures 6.5 and 6.6. The results from this algorithm are very similar those of Sheng and Hay, though as seen in the size profiles, extend farther from the bottom into regions of much lower concentration.

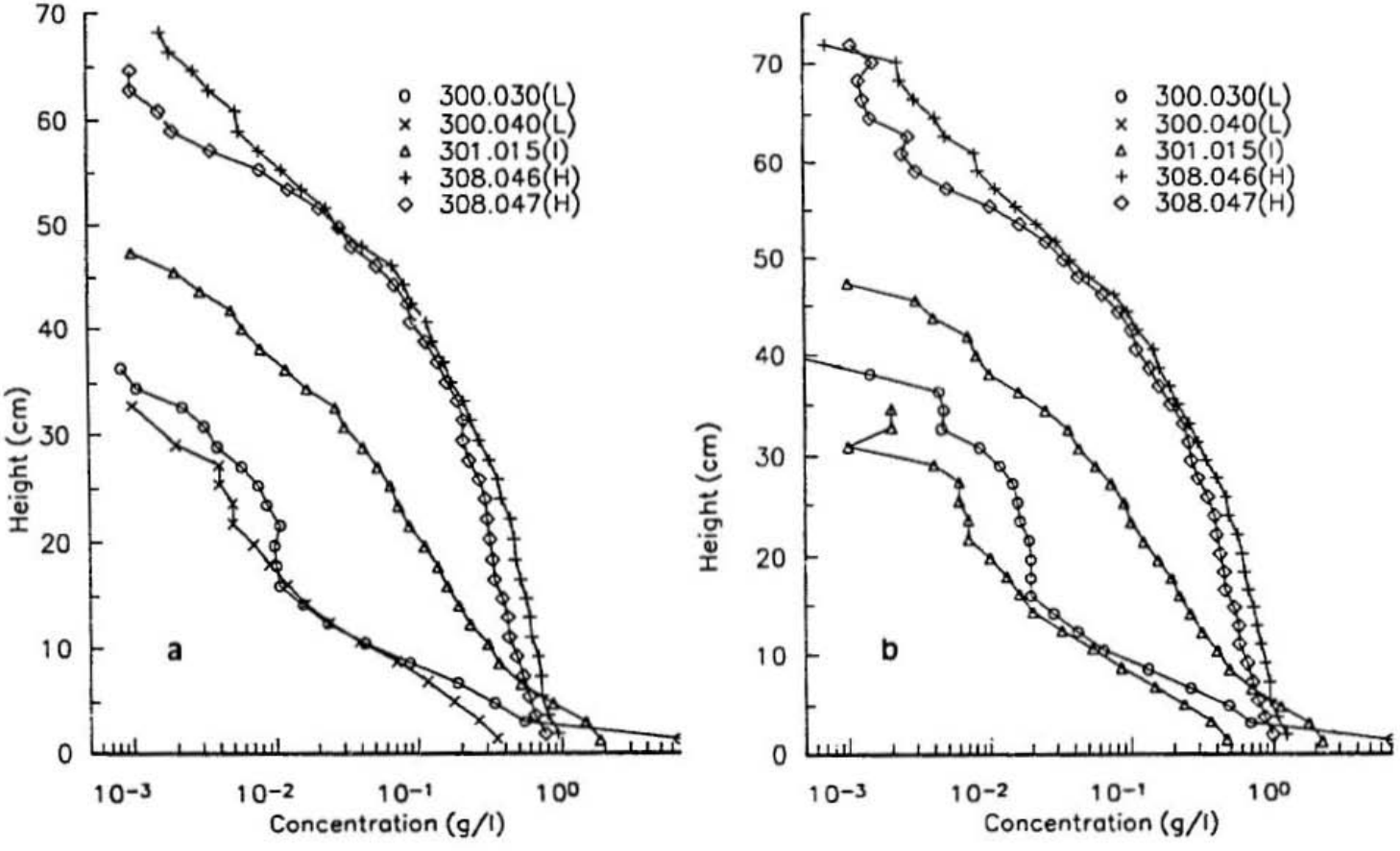

Figure 6.5: Averaged vertical profiles of concentration using the semi-empirical form factor (a) and using the rational fraction fit form factor (b). The same symbol convention as in Figures 6.2 and 6.3 has been used.

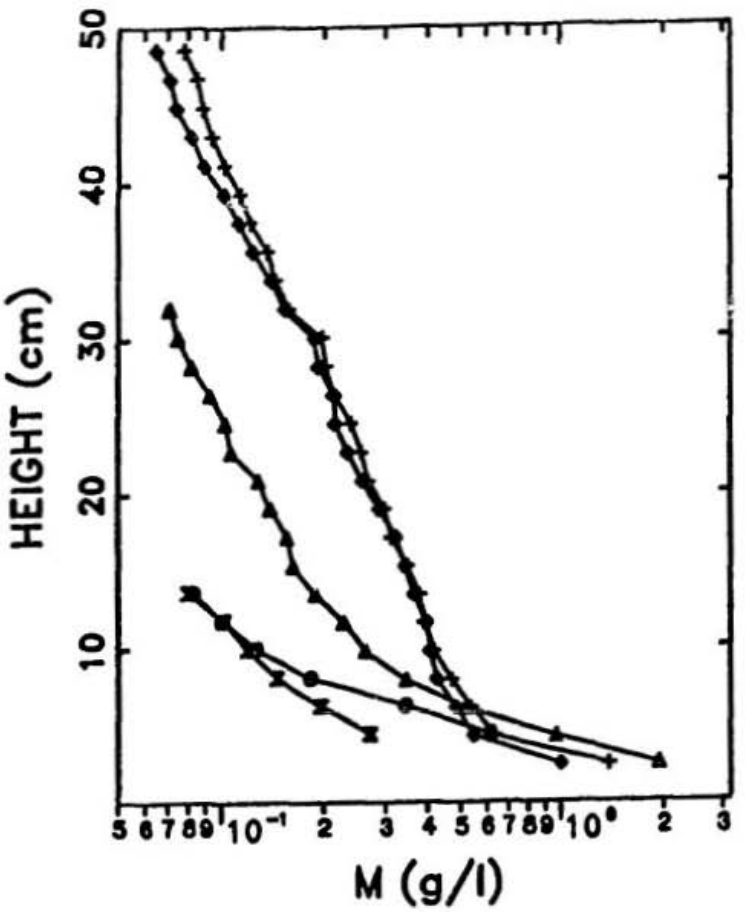

Figure 6.6: Similar concentration profiles from Sheng's inversion algorithm [from Sheng and Hay, 1991].

Subtraction of a background level from the raw voltage in the newer results has reduced the increase in concentration toward the bottom below 10 cm height seen in Sheng and Hay's profiles. The method of determining this background level could lead to inaccuracy in these inverted values very near the bottom, independent of the previously mentioned bottom echo contamination. The "quiet" periods chosen as being representative inevitably include a small amount of suspended sand in the near-bottom layer. The profiles from Sheng and Hay [1991] show two distinct regions: below 10 cm, where concentration decreases non-exponentially with height, and above 10 cm, where decrease in concentration is exponential. The newer results show a third region in the high energy cases above 40 cm where concentration decreases more quickly with height than in the 10-40 cm region.

Figure 6.7 shows profiles of concentration and size which represent the average over four 6.5 minute runs (299.025 - .028) during intermediate energy wave conditions. Error bars in Figures 6.8 and 6.9 denote plus or minus one standard error in μm or g/l; the average of the standard error in the four individual runs has been divided by $\sqrt{4}$. The size profiles are similar to those for the intermediate energy run presented earlier (301.015). There is increased vertical range over Sheng's results, however, the size is approximately constant with height. As before, the sizes estimated using

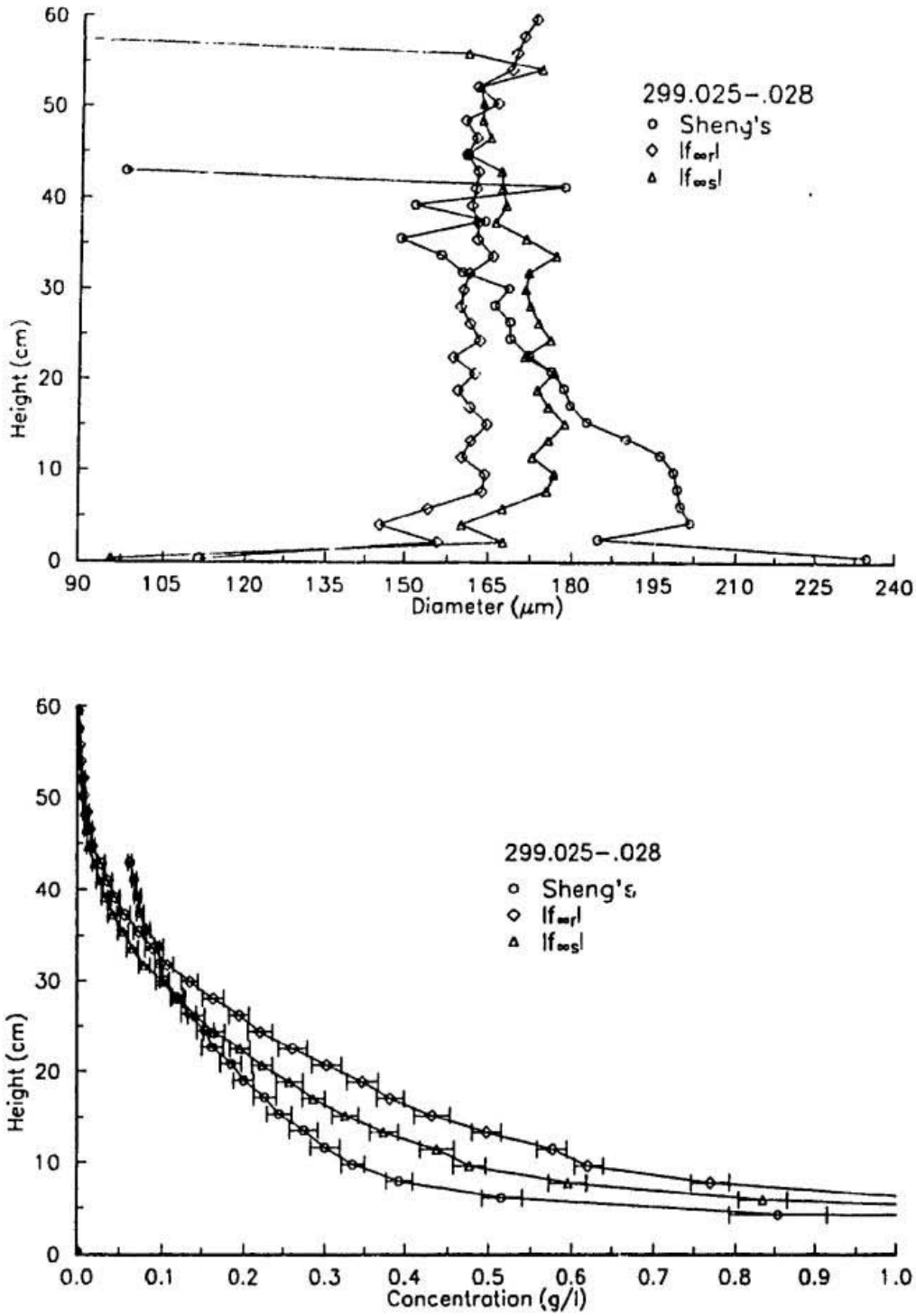

Figure 6.7: 4-run averaged profiles of size and concentration for runs 299.025-.028 using both form factors and Sheng's results.

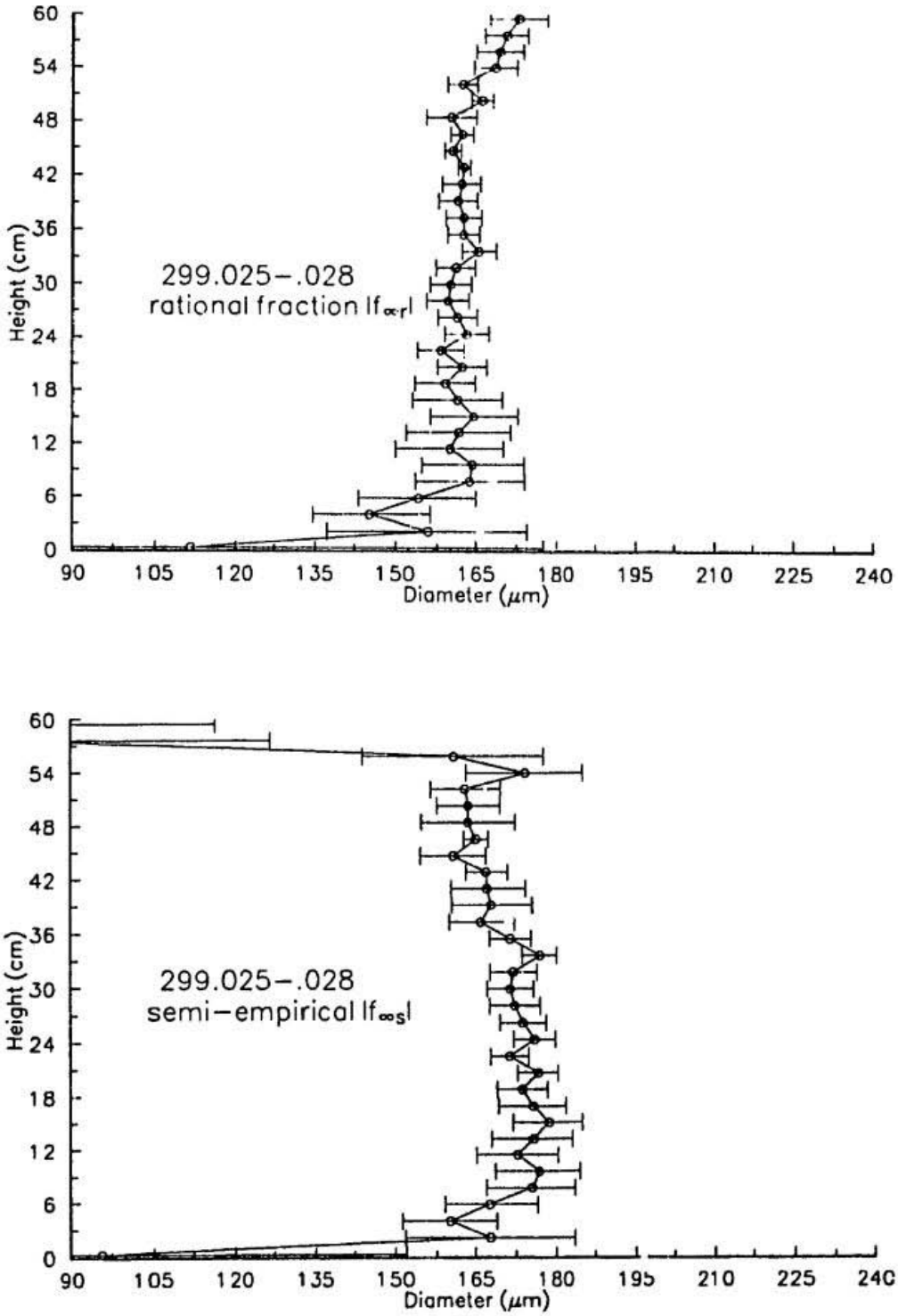

Figure 6.8: 4–run averaged profiles of size with error bars denoting plus or minus one standard error for runs 299.025–.028 using both form factors as labelled.

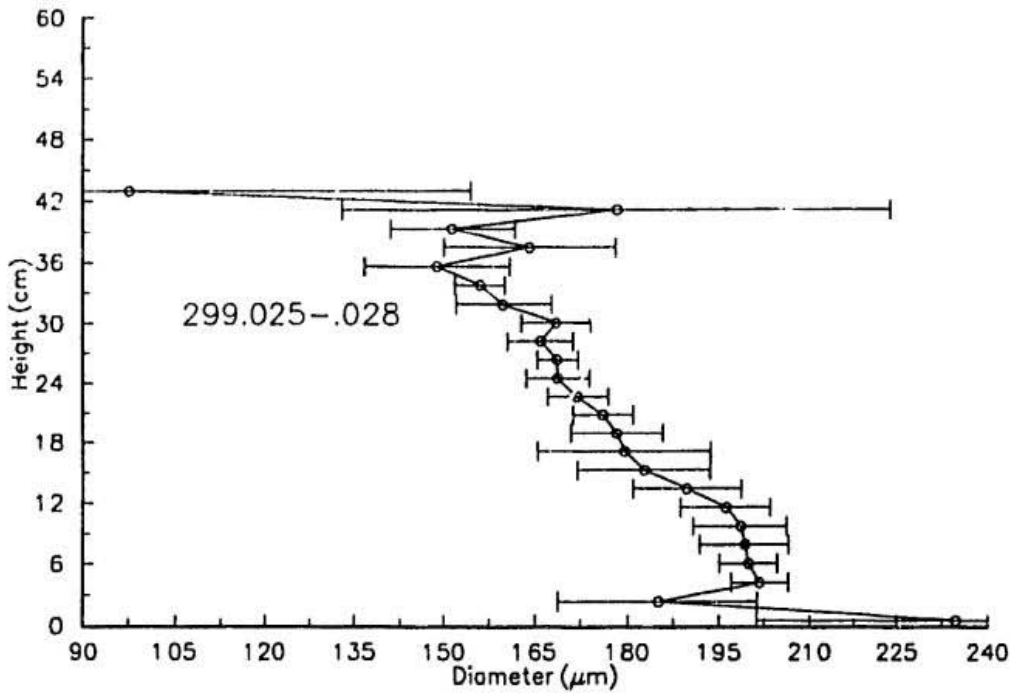

Figure 6.9: 4-run averaged profile of size from Sheng's algorithm with error bars denoting plus or minus one standard error.

the semi-empirical form factor are larger than those using the rational fraction form factor. The standard error in size is similar for the two different form factors, and in both cases, is less than for the results from Sheng and Hay. Averaging over 4 runs has reduced the standard error to less than 7% between 5 and 50 cm in height.

The concentration profiles show small error in all cases. In the region above 35 cm height, the effect of subtraction of a background level from the voltage data (in the newer algorithm) is evident in reduced concentrations. Below 35 cm height, concentrations estimated by the new algorithm are larger than those from Sheng and Hay, with the rational fraction fit form factor results about 30% larger than the results using the semi-empirical form factor. For a sand size of 165 μm, $X = 0.35$ at 1 MHz, where $|f_{\infty s}| < |f_{\infty r}|$ by approximately 5%, $X = 0.79$ at 2.25 MHz and 1.75 at 5 MHz, where $|f_{\infty s}| > |f_{\infty r}|$ by approximatley 10% (see Figure 3.4). This moves the ϵ_{31} curve up for the rational fraction fit form factor case, which shifts the zero crossing to the left (refer to Figure 4.2a), resulting in a smaller value. The same reasoning applies to the ϵ_{21} (the size being less than 280 μm).

Figure 6.10 shows the difference as a function of height between the averaged estimates made using the two form factors: [(with $|f_{\infty s}|$) - (with $|f_{\infty r}|$)]/(with $|f_{\infty s}|$). The difference in size is approximately constant at

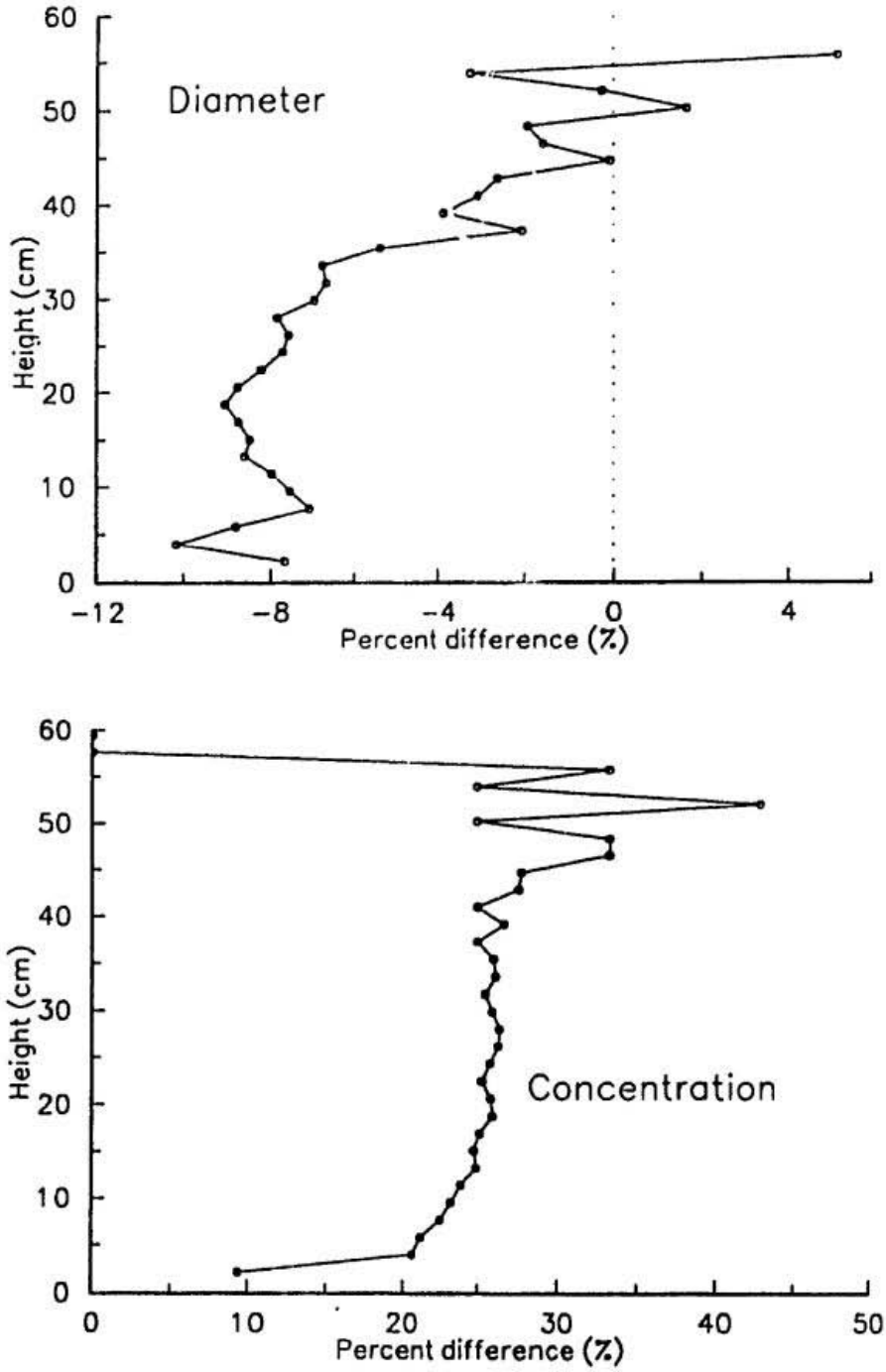

Figure 6.10: Percent difference between size and concentration estimates using the two different form factors.

about -8% up to a height of 30 cm. Where estimation becomes more erratic in regions of smaller concentration, the difference rises, though fluctuating, to near zero (excluding the large positive value at the top of the profile). This difference is carried through to the concentration profile: difference is approximately constant at 25% over the same range of height. In the concentration estimates, the effect of the percent difference in size estimates combines with the difference in the form factors to produce an even larger spread between the two sets of results. An approximately -10% difference between the two fitted form factors at 2 of the 3 operating frequencies leads to a similar (-8%) difference in size estimates, and a much larger (25%) difference in concentration estimates. It is interesting that, though the form factor contributes *size* dependence to the backscatter formulation, differences in the functional form of the backscatter form factor have larger impact on *concentration* estimation.

Chapter 7

Conclusions

The inversion algorithm that has been developed shows promise and improvement over the ratio algorithm in some areas. The comparison between the two inversion approaches has highlighted some areas where further investigation is necessary.

Comparison of inverted and measured laboratory data shows that the inversion algorithm is reasonably accurate over the range of particle sizes used in the experiments (98 to 463 μm) up to concentrations of 10 g/l. The most significant result arising from the examination of the laboratory data is the identification of large over-correction by the scattering attenuation term. The calculated values shown in Figure 5.5 are twice as large as measured

values. Preliminary results of ongoing research show that the ratio algorithm *under*-corrects for scattering attenuation. This would indicate that part of the problem lies in the use of $< v^2 >$, as opposed to $< v >$. Note that the strategy employed in this new inversion method does not depend on the use of $< v^2 >$: it would be worthwhile to develop a version of this algorithm using mean voltages instead of the mean square voltages, as well as more efficient zero-finding to improve computation time. In any case, implementation of another frequency less sensitive to scattering attenuation, i.e. less than 5 MHz, would be advantageous in resolving this question.

The extent of the effect of the scattering geometry on inversion of the laboratory data is another interesting result. This has implications which are specific to experiments performed using the jet, though points to the separation of the transducers as a potential source of error in inverted field data.

The differences in the inverted results using two fits to the backscatter form factor measurements show that estimates of size and concentration can be sensitive to small differences in the form factor. For the particular case discussed, with sand of diameter 165 μm, an approximately 10% difference between the two form factors (mainly at 2.25 and 5 MHz) is seen to result in an 8% difference in the estimated size, and a 25% difference in the estimated

concentration. This indicates that further work toward determining the exact behavior of $|f_\infty(X)|$ for natural sand in water is needed.

Subtraction of a background signal level from the raw data results in a lower concentration level in the region near the top of the profiles than seen in Sheng and Hay's [1991] results. This approach is valuable for reducing systematic noise. However, the method which was used here in determining this background level (averaging over apparently "quiet" raw voltage profiles which may actually include some suspended material near the bottom) could lead to false size and concentration estimates close to the bottom.

A goal of this work has been to develop an alternate method of inverting backscatter data which is not as sensitive to low signal levels as the ratio technique. The half hour-averaged profiles shown in Figure 6.7 demonstrate that this has been accomplished. The inverted vertical profiles from the field data extend farther from the bottom into regions of lower concentration. As well, the standard error in size is less than 7% through most of this range when the data are averaged over this longer interval. In general, this error is less than for similar profiles from Sheng and Hay [1991], and the region of lower standard error extends over a larger vertical range than in their results. Averaging over several 6.5-minute runs is necessary to reduce the variance of the size estimates to acceptable levels.

References

Brenninkmeyer, B., In Situ Measurements of Rapidly Fluctuating, High Sediment Concentrations, *Marine Geology*, **20**, 117–128, 1976.

Carver, R. E. (ed), *Procedures in Sedimentary Petrology*, John Wiley and Sons, Inc., New York, 653 pp., 1971.

Clay, C. S. and H. Medwin, *Acoustical Oceanography*, John Wiley, New York, 1977.

Crickmore, M. J. and R. F. Aked, Pump Samplers for Measuring Sand Transport in Tidal Waters, Conference on Instrumentation in Oceanography, University College of North Wales, Bangor, *IERE Conf. Proc. No. 32*, 311–326, 1975.

Downing, J. P., R. W. Sternberg, and C. R. B. Lister, New Instrumentation for the Investigation of Sediment Suspension Processes in the Shallow Marine Environment, *Marine Geology*, **42**, 19–34, 1981.

Faran, J. J., Jr., Sound Scattering by Solid Elastic Cylinders and Spheres, *J. Acoust. Soc. Am.*, **23**, 405–418, 1951.

Flammer, G. H., Ultrasonic Measurement of Suspended Sediment, Geo. Survey Bull. No. 1141–A (US GPO, Washington, DC), 1962.

Hanes, D. M. and D. A. Huntley, Continuous Measurement of Suspended Sand Concentration in a Wave Dominated Nearshore Environment, *Continental Shelf Research*, **6**(4), 585–596, 1986.

Hanes, D. M., C. E. Vincent, D. A. Huntley and T. L. Clarke, Acoustic Measurements of Suspended Sand Concentration in the C^2S^2 Experiment at Stanhope Lane, Prince Edward Island, *Mar. Geol.*, **81**, 185–196, 1988.

Hay, A. E., On the Remote Acoustic Detection of Suspended Sediment at

Long Wavelengths, *J. of Geophysical Res.*, **88**(C12), 7525–7542, 1983.

Hay, A. E., Sound Scattering from a Particle-Laden, Turbulent Jet, *J. Acoust. Soc. Am.*, **90**(4), Pt. 1, 2055-74, 1991.

Hay, A. E. and A. J. Bowen, Acoustic Measurements of Spatially–Correlated Depth Changes in the Nearshore Zone During Autumn Storms, in preparation, 1991.

Hay, A. E. and R. W. Burling, On Sound Scattering and Attenuation in Suspensions, with Marine Applications, *J. Acoust. Soc. Am.*, **72**(3), 950–959, 1982.

Hay, A. E., L. Huang, E. B. Colbourne, J. Sheng and A. J. Bowen, A High Speed Multi-Channel Data Acquisition System for Remote Acoustic Sediment Transport Studies, in *Oceans '88 Proceedings*, IEEE, Baltimore, Vol. 2, 413–418, 1988.

Hay, A. E. and D. G. Mercer, On the Theory of Sound Scattering and Viscous Absorption in Aqueous Suspensions at Medium and Short Wavelengths, *J. Acoust. Soc. Am.*, **78**(5), 1985.

Hay, A. E. and A. S. Schaafsma, Resonance Scattering in Suspensions, *J. Acoust. Soc. Am.*, **85**(3), 1989.

Hazen, D. G., D. A. Huntley and A. J. Bowen, "UDATS: A System for Monitoring Nearshore Processes", *Proc. Oceans '87*, 993–997, 1987.

Holliday, D. V. and R. E. Peiper, Volume Scattering Strengths and Zooplankton Distributions at Acoustic Frequencies Between 0.5 and 3 MHz, *J. Acoust. Soc. Am.*, **67**(1), 135–146, 1980.

Hornbeck, R. W., *Numerical Methods*, Prentice-Hall Inc./Quantum Publishers Inc., New Jersey, 1975.

Jansen, R. H. J., An Ultrasonic Doppler Scatterometer for Measuring Suspended Sand Transport, *Ultrasonics International 79 Conference Proceedings*, Graz, Austria, **U179**, 366–371, 1979.

Jensen, J. K. and T. Sorensen, Measurements of Sediment Suspension in Combinations of Waves and Currents, from *Coastal Engineering Conference*, **2**, 1097–1104, 1972.

Johnson, R. K., Sound Scattering from a Fluid Sphere Revisited, *J. Acoust. Soc. Am.*, **61**, 375–377, 1977.

Kana, T. W., A New Apparatus for Collecting Simultaneous Water Samples in the Surf Zones, *Journal of Sedimentary Petrology*, **46**(4), 1031–1034, 1976.

Komar, P. D., *Beach Processes and Sedimentation*, Prentice–Hall Inc., Englewood Cliffs, New Jersey, 1976.

Kristensen, A. and J. Dalen, Acoustic Estimation of Size Distribution and Abundance of Zooplankton, *J. Acoust. Soc. Am.*, **80**(2), 601–611, 1986.

Libicki, C. and K. W. Bedford, The Interpretation and Evaluation of a 3-MHz Acoustic Backscatter Device for Measuring Benthic Boundary Layer Sediment Dynamics, *J. Acoust. Soc. Am.*, **85**(4), 1501–1511, 1989.

List, E. J., Turbulent Jets and Plumes, *Ann. Rev. Fluid Mech.*, **14**,189–212, 1982.

Lynch, J. F., Theoretical Analysis of ABSS data for HEBBLE, *Marine Geology*, **66**, 277–289, 1985.

Lynch, J. F. and Y. C. Agrawal, A Model–Dependent Method for Inverting Vertical Profiles of Scattering to Obtain Particle Size Spectra in Boundary Layers, *Marine Geology*, **99**, 387–401, 1991.

Lynch, J. F., T. F. Gross, B. H. Brunley and R. A. Filyo, Sediment Concentration Profiling in HEBBLE using a 1-MHz Acoustic Backscatter System, *Marine Geology*, **99**, 361–385, 1991.

Medwin, H., In Situ Measurements of Bubble Populations in Coastal Ocean Waves, *J. Geoph. Res.*, **75**(3), 599–611, 1970.

Medwin, H., In Situ Measurements of Microbubbles at Sea, *J. Geoph. Res.*, **82**, 971–976, 1977.

Morse, P. M. and K. U. Ingard, *Theoretical Acoustics*, Princeton University Press, McGraw–Hill, Inc., 1968.

Murray, S. P., Settling Velocities and Vertical Diffusion of Particles in Turbulent Water, *J. of Geophysical Res.*, **75**(9), 1647-54, 1970.

Press, W. H., B. P. Flannery, S. A. Teukolsky, W. T. Vetterling, *Numerical Recipes: The Art of Scientific Computing*, Campbridge University Press, New York, 1987.

Raleigh, Lord (J. W. Strut), *Theory of Sound*, Vol. 2, 2nd ed., 149–152, Dover, New York, 1945.

Renger, E., New Technology and Automation of Continuous Sediment Concentration Measurement. In *Transport of Suspended Solids in Open Channels*, Bechteler, W., ed., Balkema, Netherlands, 221-31, 1986.

Schaafsma, A. S. and W. J. G. J. der Kinderen, Ultrasonic Instruments for the Continuous Measurement of Suspended Sand Transport, *Proc. IAHR — Symposium on Measuring Technique in Hydraulic Research*, Delft, 11 pp., 1985.

Sheng, J., *Sound Scattering and Attenuation in Aqueous Suspensions of Sand: Comparison of Theory and Experiment*, M.Sc. thesis (Dept. of Physics, Memorial University of Nfld.), 1986.

Sheng, J., *Remote Determination of Suspended Sediment Size and Concentration by Multi-frequency Acoustic Backscatter*, Ph.D. thesis (Dept. of Physics, Memorial University of Nfld.), 1990.

Sheng, J. and A. E. Hay, An Examination of the Spherical Scatterer Approximation in Aqueous Suspensions of Sand, *J. Acoust. Soc. Am.*, **83**(2), 598-610, 1988.

Sheng, J. and A. E. Hay, Vertical Profiles of Suspended Sand Concentration and Size From Multifrequency Acoustic Backscatter, submitted to *J. Geophys. Res.*, 1991.

Sleath, J. F. A., *Sea Bed Mechanics*, John Wiley and Sons, New York, 251-325, 1984.

Soulsby, R. L., A. P. Salkield, R. A. Haine and B. Wainwright, Observations of the Turbulent Fluxes of Suspended Sand Near the Sea-bed, *Euromech 192: Transport of Suspended Solids in Open Channels*, Neubiberg, 183-186, 1985.

Staub, C., I. G. Jonsson and I. A. Svendsen, Variation of Sediment Suspension in Oscillatory Flow, *Coastal Engineering*, **3**, 2310-2321, 1984.

Thorne, P. D., Laboratory and Marine Measurements on the Acoustic Detection of Sediment Transport, *J. Acoust. Soc. Am.*, **80**(3), 899-910, 1986.

Thorne P. D., C. E. Vincent, P. J. Hardcastle, S. Rehman and N. Pearson, Measuring Suspended Sediment Concentrations Using Acoustic Backscatter Devices, *Marine Geology*, **98**, 7-16, 1991.

Varadan, V. K., V. N. Bringi, V. V. Varadan and Y. Ma, Coherent Attenuation of Acoustic Waves by Pair-Correlated Random Distribution of Scatterers With Uniform and Gaussian Size Distributions, *J. Acoust. Soc. Am.*, **73**(6), 1941-1947, 1983.

Young, R. A., J. T. Merrill, T. L. Clarke and J. R. Proni, Acoustic Profiling of Suspended Sediments in the Marine Bottom Boundary Layer, *Geophysical Res. Lett.*, **9**, 175-178, 1982.